ELASTIC ELECTRON SCATTERING OFF ^{3}He AND ^{4}He AT LARGE MOMENTUM TRANSFERS

Jefferson Lab PAC25 Proposal

December 2003

J. R. Arrington

Argonne National Laboratory, Argonne, IL 60439

K. A. Aniol, M. B. Epstein, D. J. Margaziotis

California State University, Los Angeles, CA 90032

W. Boeglin, P. E. C. Markowitz

Florida International University, Miami, FL 33199

R. De Leo, L. Lagamba

INFN/Bari and University of Bari, 70126 Bari, Italy

F. Cusanno, S. Frullani, F. Garibaldi, M. Iodice, G. M. Urciuoli

INFN/Sanità and ISS Physics Lab., 00161 Rome, Italy

J.-P. Chen, J. Gomez, D. W. Higinbotham, C. W. de Jager, S. Nanda, J. J. LeRose, B. Reitz, A. Saha

Jefferson Lab, Newport News, VA 23606

A. Adeluyi, B. D. Anderson, A. T. Katramatou, D. M. Manley, G. G. Petratos, J. W. Watson, W.-M. Zhang

Kent State University, Kent, OH 44242

E. J. Beise, C.-C. Chang

University of Maryland, College Park, MD 20742

A. Hotta, K. S. Kumar, R. A. Miskimen, G. A. Peterson, S. E. Rock
University of Massachusetts, Amherst, MA 01003

W. Bertozzi, O. Gayou, S. Gilad, R. Suleiman
Massachusetts Institute of Technology, Cambridge, MA 02139

J. R. Calarco
University of New Hampshire, Durham, NH 03824

J. A. Templon
NIKHEF, 1009 DB Amsterdam, The Netherlands

P. E. Ulmer
Old Dominion University, Norfolk, VA 23529

K. Kino
RCNP, Osaka University, Ibaraki, Osaka 567, Japan

L. E. Marcucci
University of Pisa and INFN/Pisa, 56127 Pisa, Italy

R. Gilman, X. Jiang, G. Kumbartzki, K. McCormick, R. D. Ransome
Rutgers, The State University of New Jersey, Piscataway, NJ 08855

A. J. Sarty
Saint Mary's University, Halifax, NS B3H3C3, Canada

P. Decowski
Smith College, Northampton, MA 01063

M. N. Olson
St. Norbert College, De Pere, WI 54115

F. Butaru, S. Choi, Z.-E. Meziani, K. Slifer, P. Solvignon, H. Yao

Temple University, Philadelphia, PA 19122

T. Tamae

Laboratory of Nuclear Science, Tohoku University, Sendai 982, Japan

B. E. Norum

University of Virginia, Charlottsville, VA 22903

D. Armstrong, T. Holmstrom, B. Moffit

College of William and Mary, Williamsburg, VA 23187

and

The Jefferson Lab Hall A Collaboration

Spokespersons: J. Gomez, A. T. Katramatou and G. G. Petratos (Contact Person)

ABSTRACT

We repropose the approved JLab experiment E00-118 on measurements of elastic electron scattering off the ^{3}He and ^{4}He few-body systems up to the highest momentum transfers possible, limited by cross section sensitivity. E00-118 was approved in 2000 for one month of beam time with A$^-$ scientific rating. The measurements will extend our knowledge of the elastic form factors of the helium isotopes down by more than one order in magnitude and out in Q^2 possibly by more than a factor of two. The experiment will use the Hall A Facility of JLab. Scattered electrons will be detected in the Electron High Resolution Spectrometer. Recoil nuclei will be detected in coincidence with the scattered electrons in the Hadron High Resolution Spectrometer. Electron-recoil nucleus coincidences will be identified by double-arm time-of-flight. The effective double-arm solid angle and radiative corrections for the evaluation of the cross sections will be determined by means of a Monte Carlo simulation. The results are expected to play a crucial role in establishing a consistent standard model describing the structure of few-body nuclei in terms of nucleons and mesons, and in possibly providing evidence for its break-down at "large" momentum transfers, where the quark-gluon degrees of freedom are expected to dominate. We request 36 days of beam time at a beam current of 100 μA for helium production data and hydrogen calibrations.

1 Introduction

Elastic electron scattering off ^{3}He and ^{4}He is one of the simplest reactions between an electromagnetic probe and the few-body nuclear systems [1]. The electromagnetic form factors of ^{3}He and ^{4}He are observables very sensitive to the choice of the nucleon-nucleon interaction potential, to the treatment of meson-exchange currents and relativistic corrections, and to a possible admixture of multi-quark states. In fact, these factors are, along with the deuteron elastic structure functions, the "observables of choice" [2] for testing the nucleon-meson standard model [3] of the nuclear interaction and the associated current operator. At large momentum transfers they may offer a unique opportunity to uncover a possible transition in the description of elastic electron scattering off the few-body systems from meson-nucleon to quark-gluon degrees of freedom as predicted by quark-dimensional scaling [4].

Experimentally, the ^{3}He charge, F_C, and magnetic, F_M, form factors and the ^{4}He charge form factor, F_C, are determined from elastic electron scattering studies with high-density targets and magnetic spectrometer systems capable of resolving elastic events with only scattered electron detection or detecting recoil nuclei also in coincidence. There have been extensive experimental investigations of the helium form factors over the past 40 years at almost every electron accelerator laboratory [5].

The cross section for elastic electron scattering from the spin one-half ^{3}He nucleus is given, in the one-photon exchange approximation, by:

$$\frac{d\sigma}{d\Omega}(E,\Theta) = \frac{(Z\alpha)^2 E'}{4E^3 \sin^4\left(\frac{\Theta}{2}\right)} \left[A(Q^2)\cos^2\left(\frac{\Theta}{2}\right) + B(Q^2)\sin^2\left(\frac{\Theta}{2}\right)\right], \tag{1}$$

where α is the fine-structure constant, Z is the nuclear charge, E and E' are the incident and scattered electron energies, Θ is the electron scattering angle, $Q^2 = 4EE'\sin^2(\Theta/2)$ is the squared four-momentum transfer, and $A(Q^2)$ and $B(Q^2)$ are the ^{3}He elastic structure functions, given in terms of the charge and magnetic form factors as:

$$A(Q^2) = \frac{F_C^2(Q^2) + (1+\kappa)^2 \tau F_M^2(Q^2)}{1+\tau}, \tag{2}$$

$$B(Q^2) = 2\tau(1+\kappa)^2 F_M^2(Q^2), \tag{3}$$

where $\tau = Q^2/4M^2$ with M being the mass of the target nucleus, and κ is the anomalous magnetic moment of the nucleus. The two form factors of ^{3}He are determined by measuring

the elastic cross section at several angles using variable beam energies for the same fixed Q^2 (Rosenbluth separation).

The cross section for elastic electron scattering from the spin zero ^{4}He nucleus is free of a magnetic contribution and is given, in the one-photon exchange approximation, by:

$$\frac{d\sigma}{d\Omega}(E,\Theta) = \frac{(Z\alpha)^2 E' \cos^2\left(\frac{\Theta}{2}\right)}{4E^3 \sin^4\left(\frac{\Theta}{2}\right)} F_C^2(Q^2). \quad (4)$$

The ^{4}He charge form factor is determined at a given Q^2 by a single angle cross section measurement using, to maximize the counting rate, the highest possible beam energy.

2 Theory and Data Review

The ^{3}He and ^{4}He form factors have been theoretically investigated using different methods to solve for the nuclear ground states: the Faddeev-Yakubovsky, the correlated-hyperspherical-harmonics (CHH) and the Monte Carlo method [3]. All three methods provide a solution of the Schrödinger equation for non-relativistic nucleons bound by a given nucleon-nucleon interaction. The Faddeev-Yakubovsky decomposition for the three- or four-body problem rewrites the Schrödinger equation as a sum of three or four equations, in which only one pair of nucleons (for two-nucleon interactions, at least) interacts at a time. The resulting equations are solved in either momentum [6, 7] or coordinate [8, 9] space. The CHH method [2] is based on the expansion of the wave function on a suitable basis of hyperspherical harmonic functions multiplied with strong state-dependent correlations, which are induced by the nucleon-nucleon interaction. The expansion coefficients are then determined applying the Rayleigh-Ritz variational principle. The two principal Monte Carlo schemes developed to study the nuclear structure of light nuclei are the variational and Green's function Monte Carlo. The variational Monte Carlo method (VMC) [10, 11, 12, 13] uses Monte Carlo techniques to perform standard numerical quadratures, while the Green's function Monte Carlo method (GFMC) [12, 14] employs Monte Carlo techniques to evaluate the imaginary-time path integrals relevant for a light nucleus.

In the simple description of the interaction between light nuclei and electromagnetic probes, the nuclear electromagnetic current operators are expressed in terms of those associ-

ated with the individual protons and neutrons [the so–called impulse approximation (IA), see Figure 1(a)]. Such a description is clearly incomplete, since the meson-exchange mechanisms, which mediate the nucleon-nucleon interaction, naturally lead to effective many-body current operators [15]. Theoretical studies of the electromagnetic form factors of the deuteron and few-body nuclei have conclusively proven that a satisfactory qualitative description of these form factors requires the inclusion of meson-exchange currents (MEC).

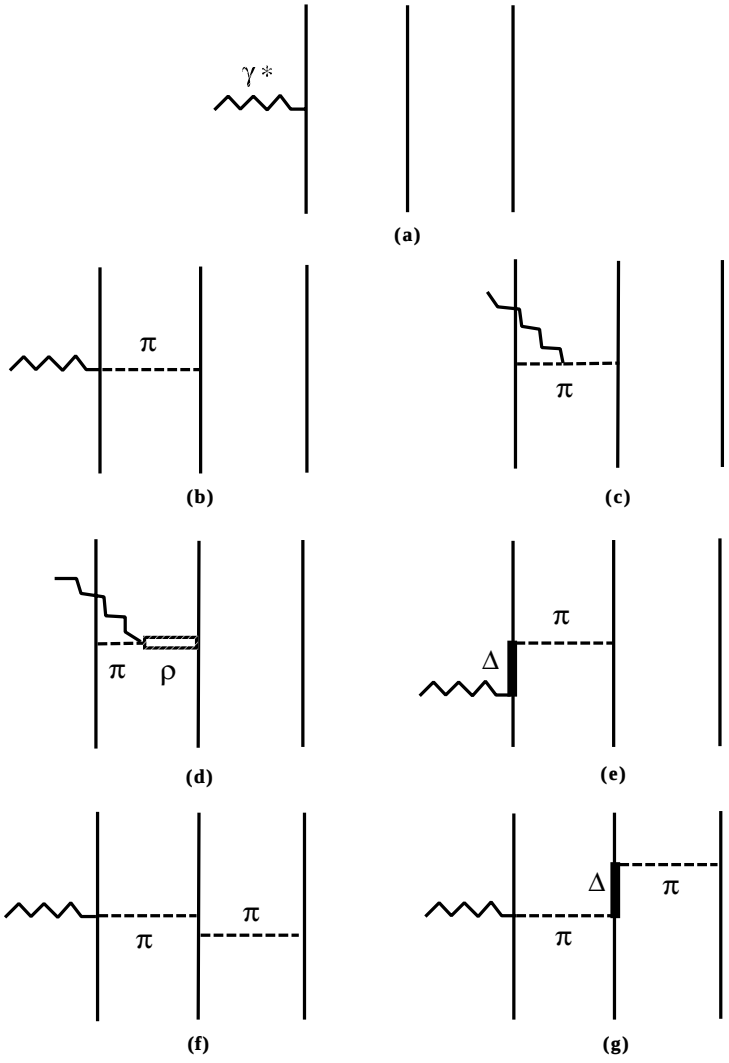

Figure 1: Selected diagrams contributing to elastic electron-^{3}He scattering: (a) impulse approximation; (b,c) "model-independent" meson-exchange currents; (d) "model-dependent" meson-exchange current; (e) "model-dependent" excitation of the Δ-isobar; (f,g) three-body currents [3].

The two-body meson-exchange currents fall into two categories. The first one includes those operators which are required by gauge invariance. Since they are directly determined from the nucleon-nucleon interaction and contain no free parameter, they are denoted as "model-independent" [isovector currents associated with "π-like" exchange, see Figure 1(b) and 1(c)]. The second category includes currents which are purely transverse and therefore are not constrained by the continuity equation. Among these operators, denoted as "model-dependent", there are the ones associated with the $\rho\pi\gamma$ and $\omega\pi\gamma$ transition mechanisms [see Figure 1(d)], as well as those due to excitation of intermediate nucleon resonances, specifically the Δ-isobar [see Figure 1(e)]. The introduction of isobar configurations in the description of the few-body systems is accomplished by approximate perturbative techniques [15], by solving the coupled-channel Schrödinger equation [16], or by a generalization of the correlation operator technique [17] in the context of variational methods. Isobar configurations have only small effects on the calculated few-body form factors [2].

The question whether three-body currents arising from the three-body interactions [18] [see Figure 1(f) and 1(g)] influence the trinucleon form factors has been re-examined in detail by Marcucci and collaborators [2]. Their study has reconfirmed that the effect of these three-body contributions on the ^{3}He form factors is rather small. A similar conclusion has been drawn by Katayama and collaborators for the charge form factor of ^{4}He [19].

An important question is whether mesonic and nucleonic degrees of freedom are sufficient for a quantitative understanding of the three- and four-body systems at large momentum transfers, where the nucleonic substructure and dynamics are generally recognized to make an increasing contribution and probably dominate. In an attempt to simultaneously incorporate the quark- and gluon-exchange mechanism at short distance and the meson-exchange mechanism at long and intermediate distances, several groups [20, 21, 22, 23, 24] have developed composite meson-nucleon and multi-quark superposition approaches in the calculation of the ^{3}He and ^{4}He form factors.

Typical models, which incorporate both nucleonic-mesonic and quark degrees of freedom are i) a hybrid quark-hadron model [23] in which the main parameter is the separation $r_\circ \sim 1$ fm between the "internal" quark-cluster region of overlapping nucleons and the "external" hadronic region, where the nucleons have little overlap and solutions to the Faddeev

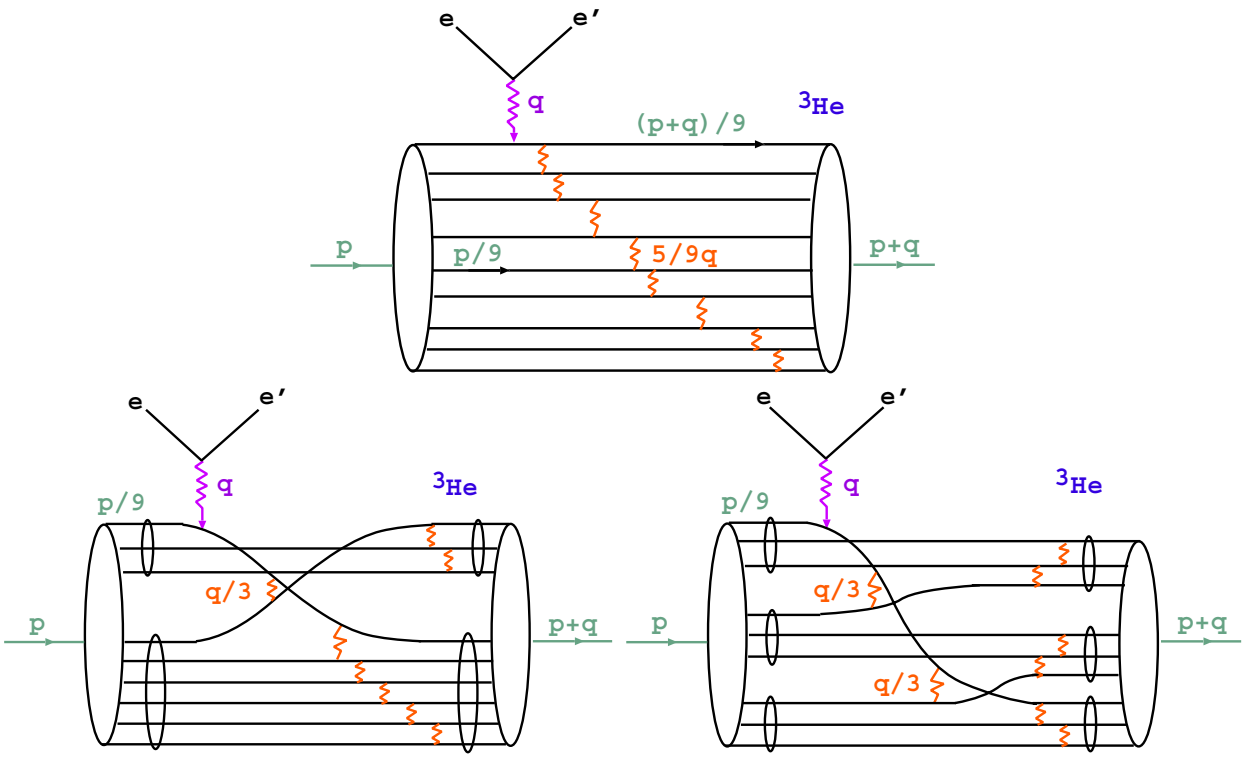

Figure 2: Elastic electron-^{3}He scattering in the dimensional-scaling quark model of Brodsky and Chertok [25]: democratic nine-quark chain (top); nucleon-dinucleon quark interchange (bottom left); three-nucleon quark interchange (bottom right).

equations are used, and ii) a multiple-quark compound model based on the relativistic harmonic oscillator quark model [22]. The hybrid models are in general able to reproduce the existing data but are still in a phenomenological stage and with sufficient freedom in the choice of elementary parameters used. The hope is that the hybrid models could provide a basis for a quantitative description of the short-distance quark structure of the few-body systems and a bridge for treating short-range phenomena with a more fundamental quantum chromodynamics prescription.

Another approach trying to incorporate the quark-gluon substructure of the helium isotopes is, as for the deuteron case, the dimensional-scaling quark model [25]. The principal idea of this model is dimensional scaling of high energy amplitudes using quark count-

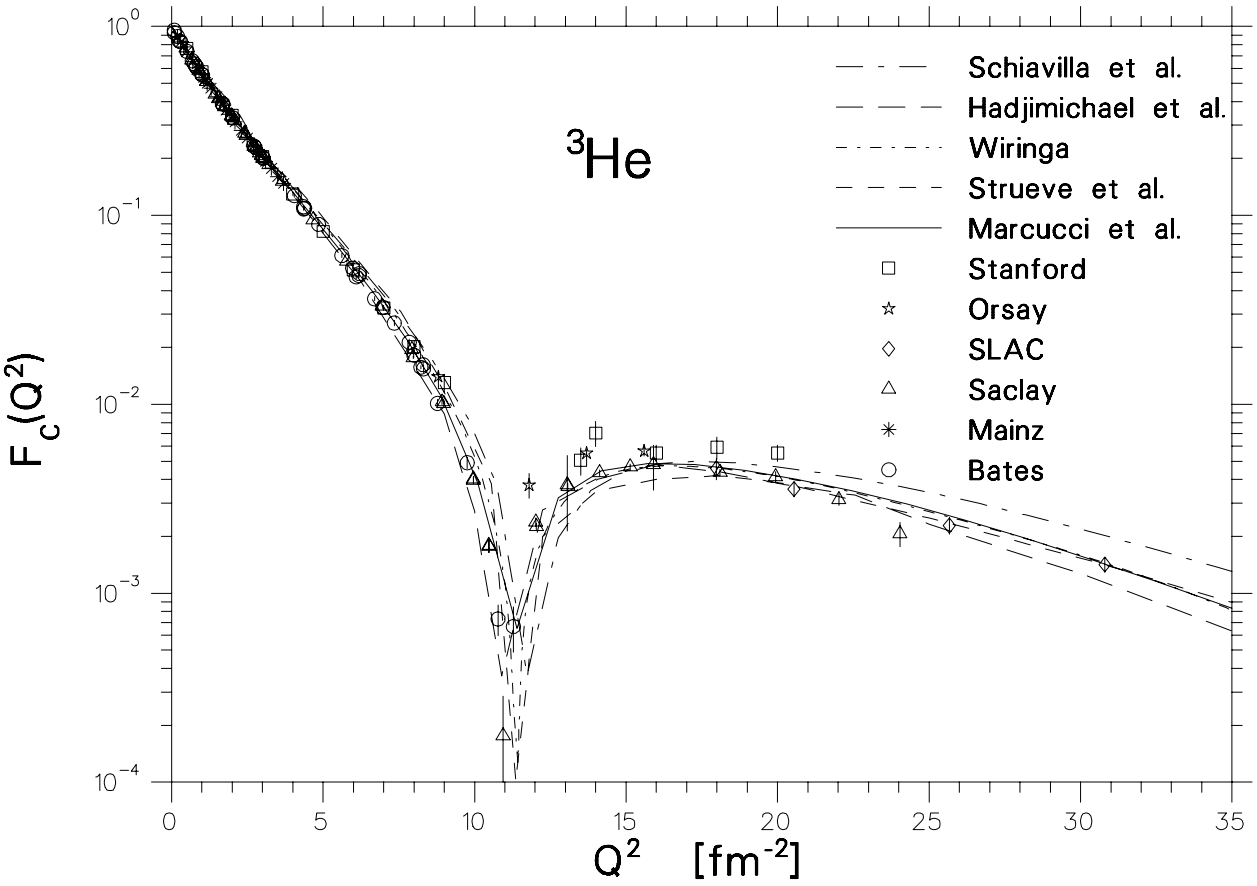

Figure 3: ^{3}He charge form factor data from Stanford [26, 27], Orsay [28], SLAC [35], Saclay [30], Mainz [34] and Bates [32] experiments, and theoretical IA+MEC calculations by Schiavilla *et al.* [11], Hadjimichael *et al.* [9], Strueve *et al.* [7], Wiringa [12] and Marcucci *et al.* [2] (see text).

ing, leading to i) the prediction for the "helium form factor" $F_{\rm He}(Q^2) \equiv \sqrt{A(Q^2)}$ that $F_{\rm He} \sim (Q^2)^{1-3A}$, where $A = 3$ (4) for ^{3}He (^{4}He), respectively, and ii) the dominance of the constituent-interchange force between quarks of different nucleons to share Q/A. The contention is that this quark-interchange model contains the important dynamics for the helium form factors at large Q^2 and is similar to, if not the same, as particular meson-exchange diagrams. The three relevant diagrams: i) democratic 9-quark chain model, ii) nucleon-dinucleon quark interchange, and iii) three-nucleon quark interchange are shown in Figure 2. Similarly the ^{4}He form factor can be described as a chain of twelve quarks or a skeletal four-nucleon structure, neutron-^{3}He or deuteron-deuteron with quark interchanges.

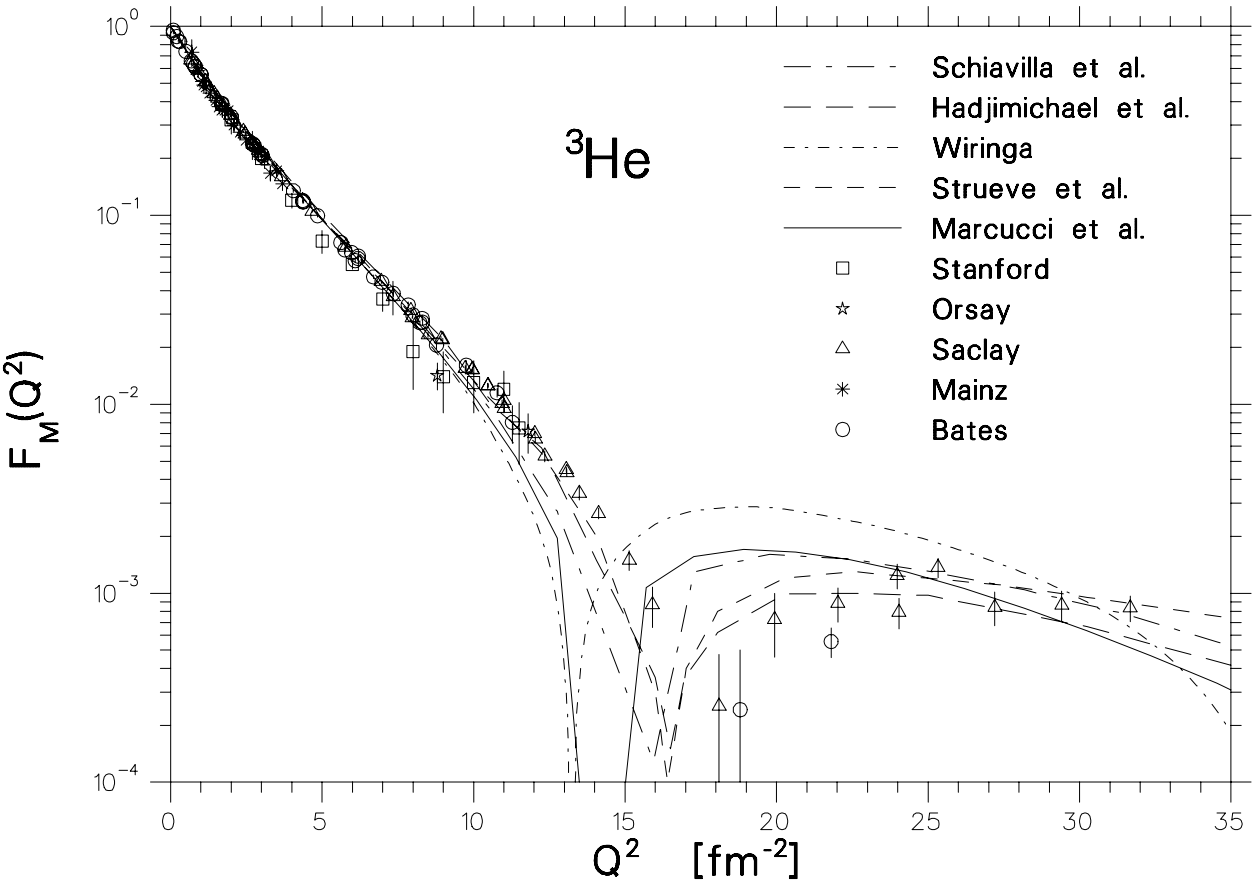

Figure 4: ^{3}He magnetic form factor data from Stanford [26, 27], Saclay [29],[30], Mainz [34], Orsay [28] and Bates [31, 33] experiments, and theoretical IA+MEC calculations by Schiavilla *et al.* [10], Hadjimichael *et al.* [9], Strueve *et al.* [7], Wiringa [12] and Marcucci *et al.* [2] (see text).

Figures 3 and 4 show all the experimental data for the ^{3}He charge and magnetic form factors in the Q^2 range 0 to 35 fm^{-2} from Stanford [26, 27], Orsay [28], Saclay [29, 30], Bates [31, 32, 33], Mainz [34] and SLAC [35] experiments. The data demonstrate the presence of an expected diffraction minimum for both form factors. They are compared to four "full" older calculations by Hadjimichael and collaborators [9], Strueve and collaborators [7], Schiavilla and collaborators [10, 11] and Wiringa [12], and a newer calculation by Marcucci and collaborators [2]. All calculations include, in addition to the impulse approximation, meson-exchange currents and genuine three-body force effects. The theoretical impulse approximation, not shown in the Figures, totally fails to describe the data. It

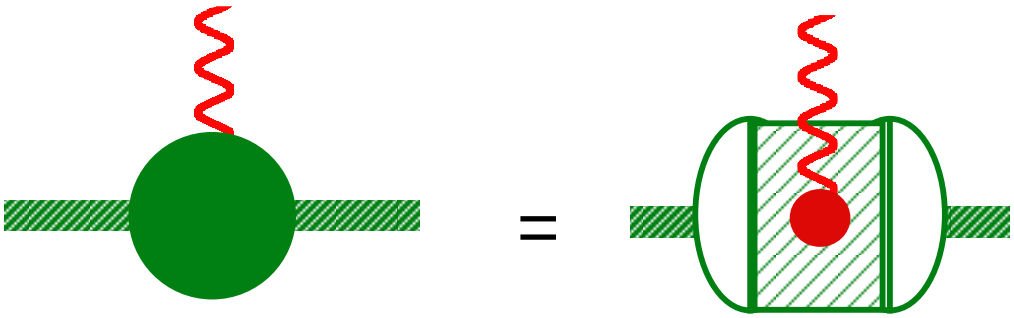

Figure 5: Diagrammatic description of the three-body bound form factor in the covariant spectator model of Gross and collaborators [39]. The shaded box, sandwiched between the half circles denoting the initial and final bound states, represents the "core" diagrams of the photon interaction with the three-body system as pictured in Figure 6.

grossly overestimates (underestimates) the location of the diffraction minimum and underestimates (overestimates) the secondary maximum of F_C (F_M), necessitating the need for inclusion of meson-exchange currents. The above calculations describe fairly well the charge form factor data, but fail to reproduce the position of the magnetic form factor minimum. Some authors [36] have attributed this disagreement to the need for fully relativistic calculations [37, 38] for the three-body form factors.

Gross and collaborators have initiated a serious effort to calculate the three-body form factors in a consistent relativistic framework. Their initial work [38] has been followed by a recent paper [39] where they derived a complete Feynman diagram expansion for the elastic form factor of the three-body bound state using the covariant spectator theory [40]. Their diagrammatic techniques have resulted in a three-nucleon current consistent with the three-body spectator equations and explicitly conserved. Their study of current conservation is based on a generalization of the work of Gross and Riska [41] requiring satisfaction of the Ward-Takahashi identities and a consistent inclusion of photon-nucleon couplings and interactions. The covariant spectator formalism has been applied very successfully to the description of nucleon-nucleon scattering and the deuteron bound state, the deuteron elastic form factors, and the electrodisintegration of the deuteron [42, 43]. It is the only formal-

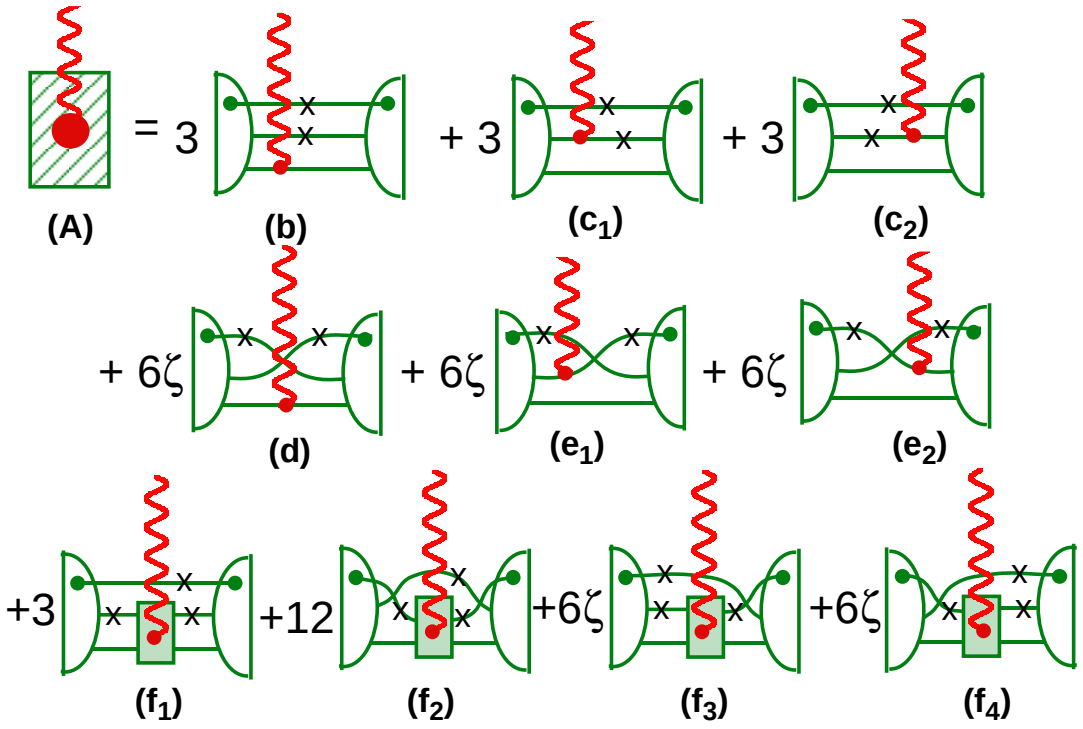

Figure 6: The "core" diagrams for the photon interaction with the three-body system in the covariant spectator model of Gross and collaborators [39] (see text). The half circles in the initial and final state can be either the bound state, or part of a three-body scattering amplitude.

ism that describes well both the electric and magnetic deuteron form factor data at large momentum transfers.

In their model, the three-body bound state form factor, shown diagrammaticaly in Figure 5, is constructed by a "core set" of diagrams, shown in Figure 6, which apply for both elastic and inelastic electron scattering off a three-nucleon system via the mediation of a virtual photon. The half circles in the initial and final state of Figure 6 can be either the bound state, or part of a three-body scattering amplitude. The crosses on the nucleon lines represent on mass-shell particles. The spectator nucleon is the one that connects to the small dot inside a half circle. Diagrams (b) through (e_2) represent direct couplings of the virtual photon to an on- or off-shell nucleon with or without exchange of the other two nucleons, and are referred to as the complete impulse approximation (CIA). Diagrams (f_1) through (f_4) showing photon

couplings inside shaded rectangles represent two-body interaction current diagrams. The calculation of the three-body form factors using the derived currents is in progress. This approach may lead to a unified consistent hadronic theory describing all electromagnetic interactions with the deuteron and the few-body nuclear systems and in particular at large momentum transfers where the non-relativistic impulse approximation framework ultimately breaks down.

Figures 7 and 8 show the predictions for the ^{3}He charge and magnetic form factors of selected IA+MEC theoretical calculations at higher momentum transfers, accessible by JLab. All calculations predict the presence of a second diffraction minimum for the ^{3}He form factors that can be observed in a JLab experiment. The location of this minimum and the height of the following maximum are very sensitive to the details of the calculations.

Figure 9 shows the available experimental data up to date for the ^{4}He charge form factor from Stanford [27, 44], Mainz [34] and SLAC [35] measurements. The data, which clearly demonstrate the presence of a diffraction minimum at $\simeq$ 10 fm^{-2}, are compared to the impulse approximation and complete (IA+MEC) calculations by Wiringa [12], Schiavilla *et al.* [11] and Marcucci *et al.* [45]. As in the case of ^{3}He, the impulse approximation alone cannot describe the data, overestimating the location of the diffraction minimum and underestimating the height of the secondary maximum. Although the inclusion of meson-exchange currents brings the theory in fair agreement with the data, it should be noted that none of the full calculations can describe, at the same time, both the Stanford and SLAC data.

Hadjimichael and collaborators [9] calculated the ^{3}He form factors solving the coupled-channel Faddeev equations in coordinate space, with several nucleon-nucleon potential models, and in particular with the Paris and Reid Soft Core potentials. The calculation included π, ρ, ω, $\rho\pi\gamma$ and $\omega\pi\gamma$ meson-exchange currents plus isobar admixtures in the initial ground state wave function. Also included are the one-body Darwin-Foldy (DF) and spin-orbit (SO) relativistic corrections to the charge operator. Three-body force effects have been accounted by including in the calculation the two-pion exchange three-body interaction, via Δ-isobar excitation.

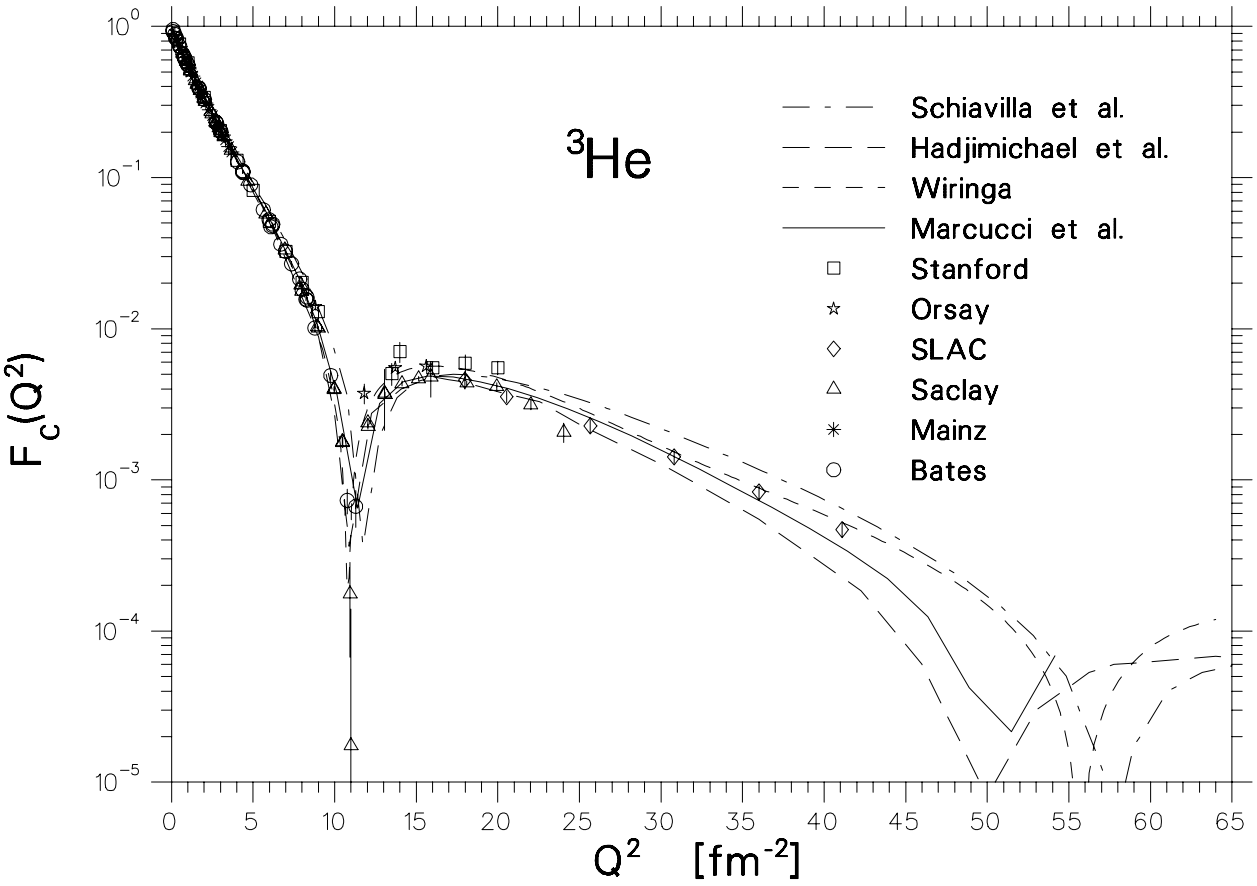

Figure 7: ^{3}He charge form factor data from Stanford [26, 27], Orsay [28], SLAC [35], Mainz [34], Saclay [30] and Bates [32] experiments, and theoretical IA+MEC calculations, for large Q^2, by Schiavilla *et al.* [11], Hadjimichael *et al.* [9], Wiringa [12] and Marcucci *et al.* [2] (see text).

Strueve and collaborators [7] calculated the ^{3}He form factors solving the Faddeev equations in momentum space, and using the Paris nucleon-nucleon potential modified to include Δ-isobar excitations via π and ρ meson-exchanges. The presence of the Δ thus accounted for the most important part of three-body force effects. The calculation included π, ρ, and $\rho\pi\gamma$ meson-exchange contributions, as well as the DF and SO relativistic corrections to the charge operator.

Schiavilla and collaborators [10, 11] calculated the ^{3}He and ^{4}He form factors using VMC wave functions computed with the Argonne v_{14} two-nucleon and the Urbana-VII three-nucleon interactions. The leading isovector meson-exchange currents, the "π-like" and "ρ-

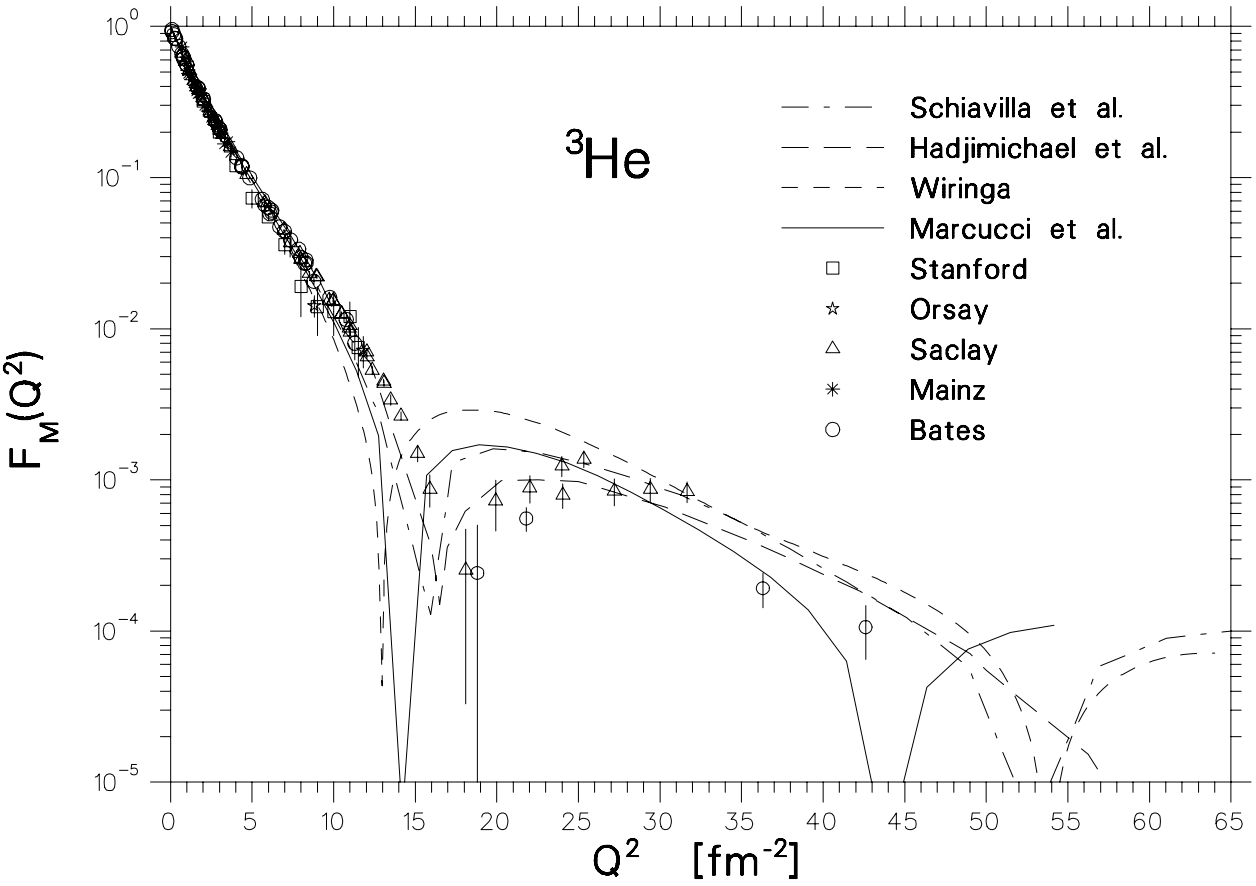

Figure 8: ^{3}He magnetic form factor data from Stanford [26, 27], Saclay [29],[30], Mainz [34], Orsay [28] and Bates [31, 33] experiments, and theoretical IA+MEC calculations, for large Q^2, by Schiavilla *et al.* [10], Hadjimichael *et al.* [9], Wiringa [12] and Marcucci *et al.* [2] (see text).

like", have been derived consistently with the nucleon-nucleon interaction used. The calculation included, in addition to the DF and SO relativistic corrections, contributions from ω and $\omega\pi\gamma$ meson-exchange charge operators.

Wiringa's calculations [12] for the ^{3}He form factors were based on the same MEC model used by Schiavilla *et al.*, and on the Argonne v_{14} potential. The ^{3}He wave functions were determined with the Faddeev equations and three-body force effects were accounted with the Urbana-VIII three-nucleon force model. The ^{4}He charge form factor was evaluated with a Monte Carlo variational wave function and a Green's function Monte Carlo wave function. The latter wave function is a v_{14} potential upgraded calculation by Carlson [14].

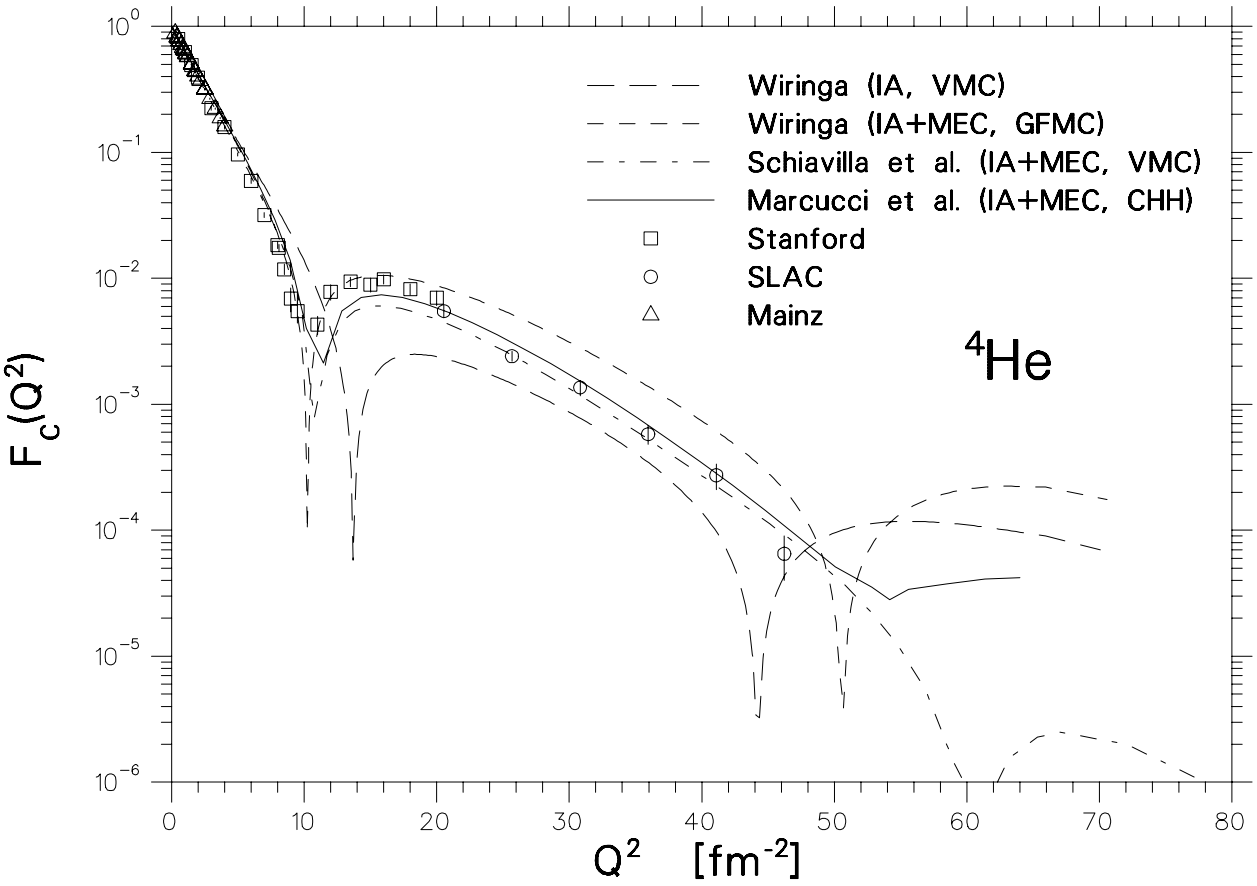

Figure 9: ^{4}He charge form factor data from Stanford [27, 44], Mainz [34] and SLAC [35], and variational Monte Carlo (VMC), Green's Function Monte Carlo (GFMC) and correlated-hyperspherical-harmonics variational method (CHH) calculations by Schiavilla *et al.* [11], Wiringa [12] and Marcucci *et al.* [45], respectively.

The most recent calculation by Marcucci and collaborators for ^{3}He [2] and ^{4}He [45] used the CHH variational method to construct high-precision wave functions obtained with the Argonnne v_{18} two-nucleon [46] and Urbana-IX three-nucleon interactions model [47]. In this calculation, the two-body MEC operators have been constructed by the same method of the earlier calculation by Schiavilla *et al.* [10, 11] and significant new advances have been made in the construction of the irreducible three-nucleon exchange current operator and in the systematic treatment of Δ-isobar configurations in the nuclear bound states.

3 The Proposed Experiment

The objective of this proposal is to improve the quality of the existing data, where possible, and most importantly to extend the measurements of the ^{3}He and ^{4}He form factors to higher momentum transfers, where the standard meson-nucleon model predicts the presence of a second diffraction minimum for all three form factors in the kinematic regime accessible by the JLab Hall A Facility. The theoretical calculations are increasingly sensitive with Q^2 to the details of the nucleon-nucleon force and to the contributions of meson-exchange currents. Precision measurements of the helium form factors at large momentum transfers will be critical in establishing the parameters of the few-body standard model, testing our knowledge of the nucleon-nucleon potential, possible three-body force effects and the nature of meson-exchange currents. The measurements can also uncover a possible transition from the standard meson-nucleon model to a quark-gluon description of the few-body form factors, as predicted by quark-dimensional scaling, if it occurs in the four-momentum range accessible by this experiment. It should be noted that measurements of the helium form factors are an integral part of the recent NSF/DOE Long Range Plan which calls explicitly for their extension to the highest possible values of momentum transfers [48]. The luminosity of the experiment will be sufficient to discover the predicted second diffraction minima of the form factors or track an asymptotic fall off in their absence.

We propose to measure using the two Hall A High Resolution Spectrometers (HRSs) and a cryogenic helium target system i) elastic electron scattering off ^{3}He at forward and backward electron scattering angles and perform a two-point Rosenbluth separation, with the wider possible angular range, to extract the charge and magnetic form factors of ^{3}He up to the maximum momentum transfer possible, and ii) forward elastic electron scattering off ^{4}He to extract the charge form factor of ^{4}He up to the maximum momentum transfer possible. The elastic cross section is expected to be as low as 4×10^{-41} cm^2/sr for ^{3}He and 4×10^{-42} cm^2/sr for ^{4}He, comparable to the lowest elastic cross section 8×10^{-42} cm^2/sr measured in the JLab Hall A deuteron elastic experiment E91-26 [49]. The inelastic threshold break-up is 5.4 MeV for ^{3}He and 20 MeV for ^{4}He. For the ^{3}He case, to ensure separation between elastic and inelastic scattering events, recoil nuclei must be detected in coincidence

with the scattered electrons. The ^{4}He measurements could in principle rely on detection of only scattered electrons provided that the electron HRS is masked from the target end-caps. As a precaution, since the cross section is expected to be extremely low, we plan to also detect recoil nuclei in coincidence and take simultaneously both single- and double-arm data. This strategy will allow us to cleanly identify, at the cost of a reduced solid angle, elastic events in the presence of an unexpected single-arm background. The identification of the electron-helium coincidences will rely on double-arm time-of-flight (TOF) measurements as in the E91-26 experiment on the deuteron. It is our expectation that the double-arm TOF spectra for this experiment will be free of background as for the electron-deuteron spectra of E91-26. Figure 10 shows a representative sample of these TOF spectra (after standard timing corrections) including the lowest and highest Q^2 kinematics [50].

The natural place to perform such measurements is the Hall A Facility with its two large solid angle, high resolution spectrometers. Beam energies in the range of 0.8 to 4.4 GeV are required for the ^{3}He measurements and 2.2 to 4.4 GeV for the ^{4}He measurements. The scattered electron energy E' will be in the range of 0.5 to 4.1 GeV for the ^{3}He case and 2.1 to 4.1 GeV for the ^{4}He case. The recoil nucleus momentum P_r will be in the range of 0.9 to 1.9 GeV/c for the ^{3}He case and 0.6 to 1.7 GeV/c for the ^{4}He case. The electron scattering angle Θ will be in the range 13° to 146° for the ^{3}He case and 16° to 25° for the ^{4}He case. The recoil angle Θ_r will be in the range 13° to 75° for the ^{3}He case and 66° to 78° for the ^{4}He case. An indicative detailed kinematic list is given, along with the ratio of the electron to recoil nucleus solid angle Jacobian, $(\Delta\Omega)_e/(\Delta\Omega)_r$, in appended Tables 1, 2 and 3.

The electron detection system will use the electron HRS detector package consisting of a drift chamber set for the momentum and angular reconstruction of the scattered particles, a Čerenkov counter and a segmented electromagnetic calorimeter for electron identification, and two planes of scintillation hodoscopes for triggering and TOF measurements. The candidate electron signal used for triggering and for double-arm TOF measurements will be the coincidence of the signals of the two scintillator hodoscopes.

The recoil nucleus detection will require a subset of the full hadron HRS detector package. The two planes of scintillators and the drift chambers will suffice for TOF measurements and for the reconstruction of the recoil nucleus momentum and recoil angle. The candidate

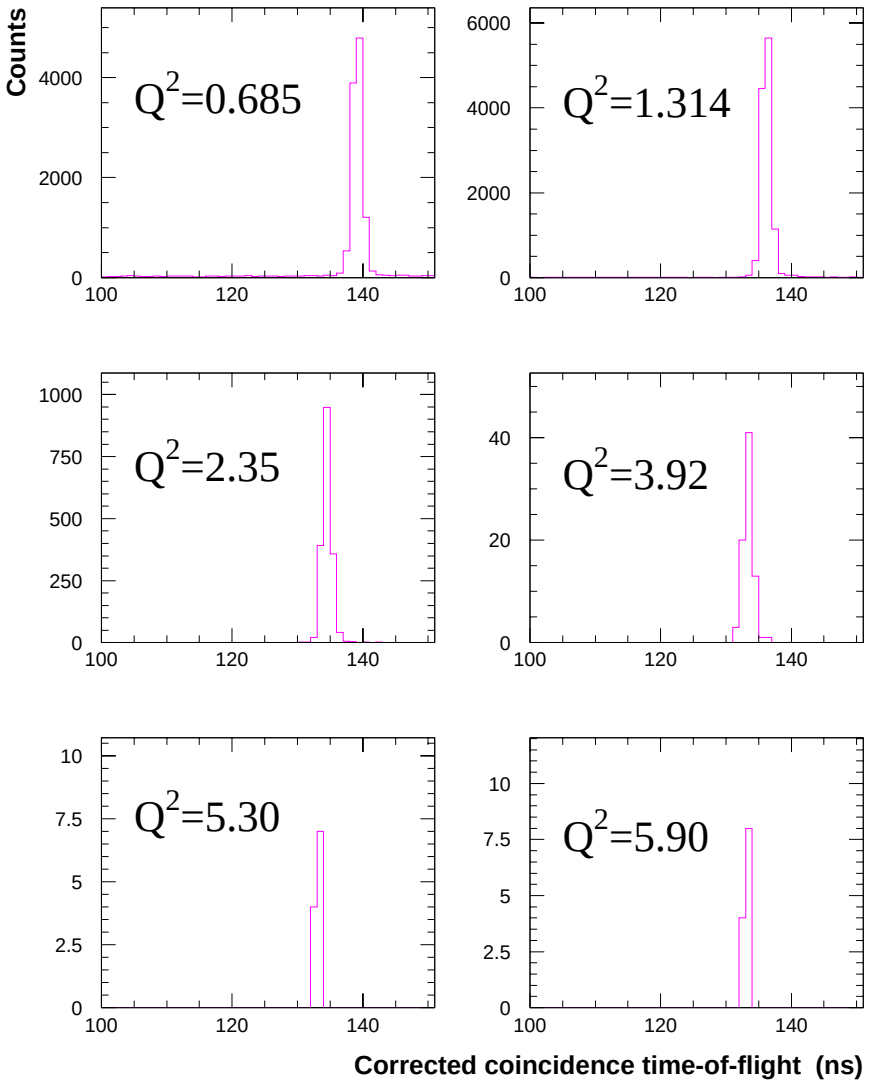

Figure 10: Electron-deuteron coincidence TOF spectra for six Q^2 kinematics (including the lowest and highest ones) from JLab Hall A elastic electron-deuteron scattering experiment E91-26, after applying standard timing corrections [50].

helium signal used for triggering and for double-arm TOF measurements will be formed by the coincidence of the signals of the two scintillator planes. To minimize absorption of recoil nuclei, not-needed detectors will be pushed to the side of the detector hut as was done in the elastic electron-deuteron measurements of E91-26.

The target system assumes three 20 cm long cells, two filled with 5 K/15 atm gas ^{3}He and ^{4}He, and one filled with liquid hydrogen. Such cells have been constructed and successfully tested by the California State University Hall A group. The ^{3}He and ^{4}He densities under these operating conditions are 0.09 g/cm^3 and 0.15 g/cm^3, respectively. The resulting luminosities for a canonical beam current of 100 μA are 2.2×10^{38} cm^{-2}s^{-1} for ^{3}He and 2.8×10^{38} cm^{-2}s^{-1} for ^{4}He. To eliminate background electrons from quasielastic scattering off the Al end-caps of the ^{4}He target cell, two adjustable tungsten collimating slits will be mounted on the support frame of the target cell towards the electron spectrometer side. The slits will mask the spectrometer from the end-caps and at the same time they will define the effective target length seen by the spectrometer.

The calibration of the single- and double-arm experimental setup will be checked and monitored with single-arm and double-arm electron-proton elastic scattering. The most important check will be the confirmation of our knowledge of the double-arm solid angle for the elastic helium measurements. Elastic electron scattering from hydrogen will be measured at every kinematical point of elastic electron-helium scattering. The electron-proton kinematics for the double-arm scattering will be such as to match as closely as possible the electron-helium solid angle Jacobian. This will constitute a powerful means of controlling the normalization of the double-arm electron-helium scattering.

The double-arm effective solid angle for the determination of the cross sections will be determined by means of a Monte Carlo simulation method of elastic electron-nucleus scattering [51] with the two HRS spectrometers. A brief essential description of the simulation method is given in the Appendix. The elastic cross section for the central values $E_\circ$ and $\Theta_\circ$ will be determined as:

$$\frac{d\sigma}{d\Omega}(E_\circ, \Theta_\circ) = \frac{N_{er}}{N_b \; N_t \; C \; F(Q^2, T) \; P_{MC}}, \tag{5}$$

where N_{er} is the number of electron-recoil nucleus coincidence events, N_b is the number of incident beam electrons, N_t is the number of target nuclei per cm^2, C is a factor correcting for electronics and computer dead-time effects, detector inefficiencies, and absorption of recoil nuclei in the target and the detectors. The function $F(Q^2, T)$ is the portion of radiative corrections that is independent of the momentum acceptances of the spectrometers, with T

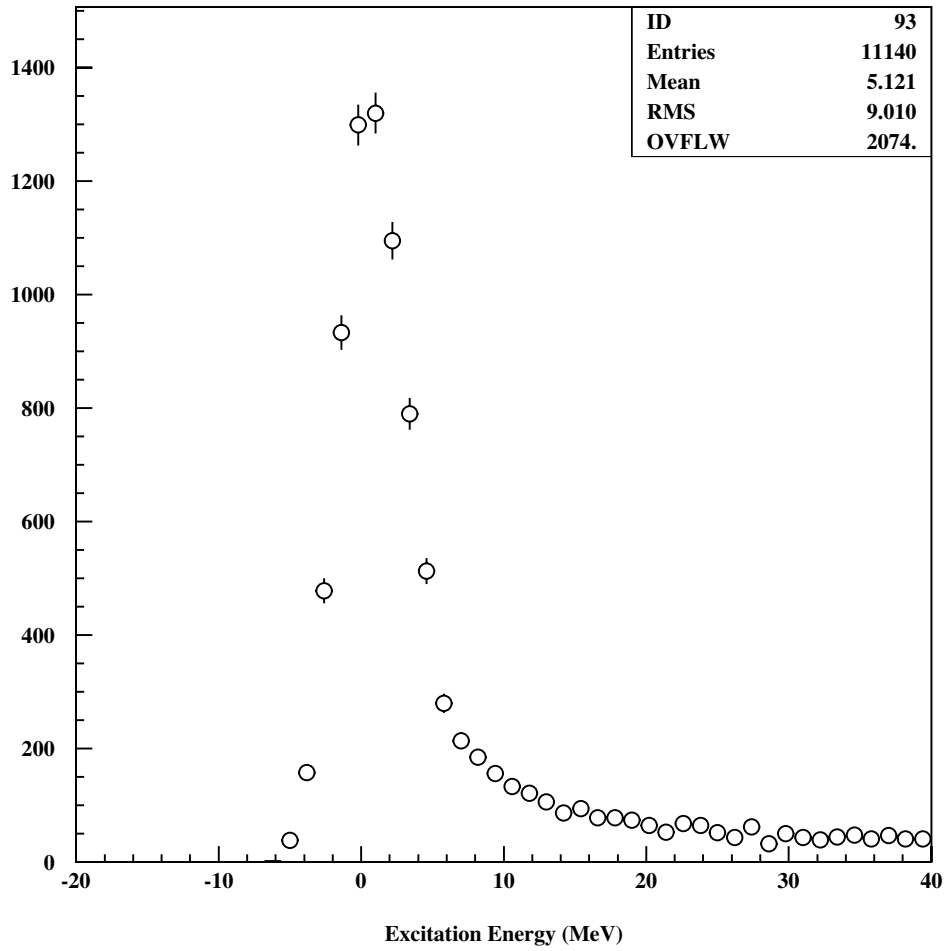

Figure 11: The excitation energy peak from our Monte Carlo simulation for the highest single-arm elastic electron-^{4}He Q^2 setting ($Q^2 = 74$ fm^{-2}). The inelastic break-up threshold is at 20 MeV.

being the total average radiator path length of the incident and scattered electrons in the target. The factor P_{MC} is the effective double-arm solid angle:

$$P_{MC} = \left\langle \int \int G(E, E', \Theta, t) d\Omega dE' \right\rangle_{E,L}, \tag{6}$$

where the function $G(E, E', \Theta, t)$ includes the momentum acceptance dependent internal and external radiative effects for the incident and scattered electrons, ionization energy losses by the electrons and the recoil nuclei, and multiple scattering effects for all particles (see Appendix). The parameter t is the position of the scattering vertex of the elastic event along

the target length L. The bracket enclosure indicates that the integral is averaged over the energy distribution of the incident beam and over the length of the target.

This Monte Carlo simulation has shown that the elastic electron-^{4}He peak of the single-arm measurements will be clearly separated from the inelastic background, as can be seen in Figure 11. Plotted in the Figure is, for the highest Q^2 kinematics (worst case), the excitation energy, $\omega = W - M$, spectrum of scattered electrons, where W is the invariant mass of the final hadronic state, $W = [M^2 + 2M(E - E') - Q^2]^{1/2}$. The excitation energy resolution will be dominated by Landau straggling in the target. Contributions from the beam energy spread and the spectrometer angular and momentum resolutions will be negligible.

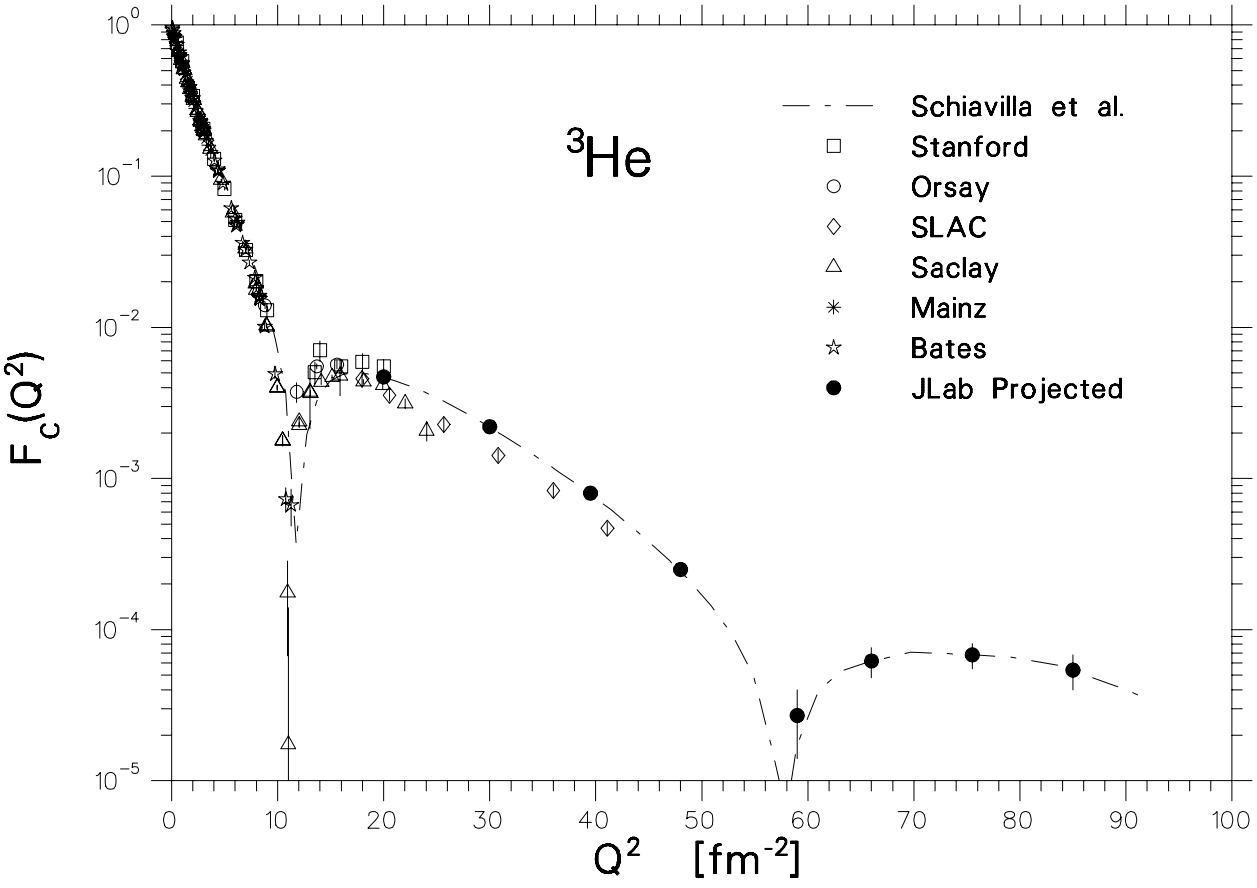

Figure 12: ^{3}He charge form factor projected data from this experiment. Also shown are data from Stanford [26, 27], Orsay [28], SLAC [35], Saclay [30], Mainz [34] and Bates [32] experiments, and the theoretical IA+MEC calculation by Schiavilla *et al.* [11].

Any possible contribution to the ^{3}He double-arm cross sections coming from the Al target end-caps will be measured in special runs with an empty replica target. It is expected, as in the case of the elastic electron-deuteron E91-26 experiment, that the hydrogen and aluminum runs will require 20% of the total running time.

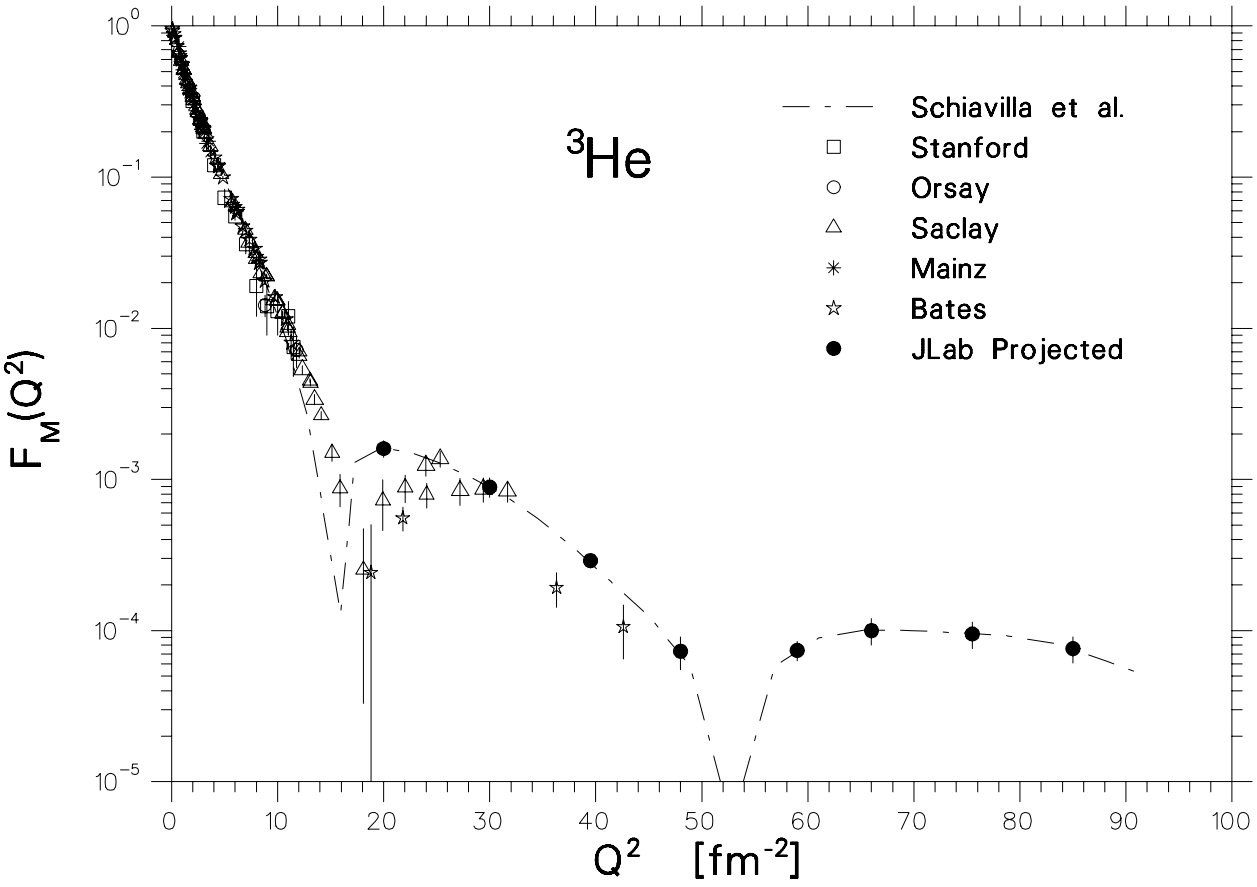

Figure 13: ^{3}He magnetic form factor projected data from this experiment. Also shown are data from Stanford [26, 27], Saclay [29, 30], Mainz [34], Orsay [28] and Bates [31, 33] experiments, and the theoretical IA+MEC calculation by Schiavilla *et al.* [10].

To calculate counting rates, projected statistical uncertainties and required beam times, we used the above stated luminosities and the full available solid angle of the two HRS spectrometers for each single- or double-arm kinematics (without using their collimators). Figures 12 and 13 show the quality of the projected data for the ^{3}He charge and magnetic form factor measurements, assuming (arbitrarily) that they are described, at large Q^2, by the

model of Schiavilla and collaborators [10, 11]. The estimated cross sections, counting rates, running times and projected statistical uncertainties in the extraction of the ^{3}He charge and magnetic form factors are given in appended Table 4.

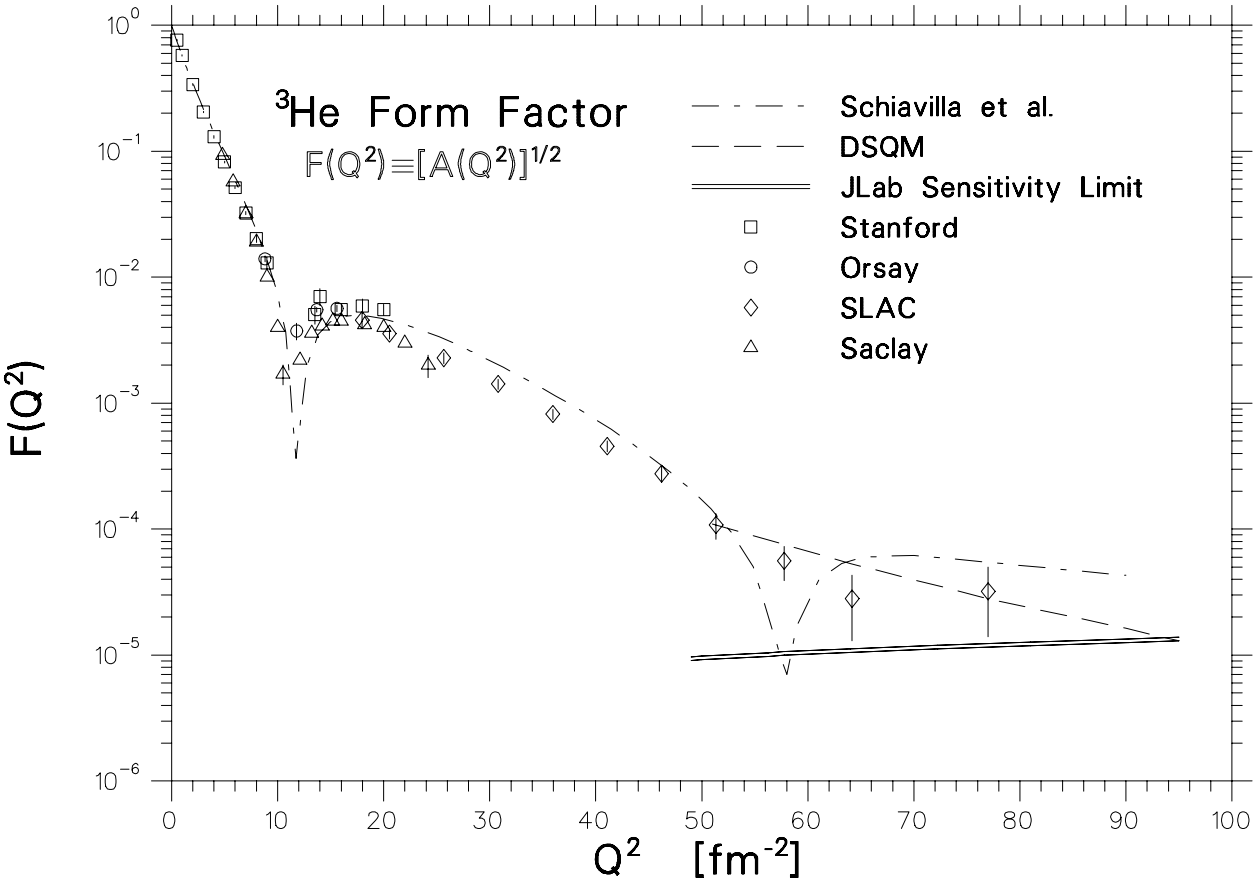

Figure 14: The sensitivity limit ($\sim \pm 30\%$ measurement in four days of beam time at a given Q^2) of this experiment for the "^{3}He form factor". Also shown are existing data from Stanford [26, 27], Orsay [28], SLAC [35] and Saclay [30] experiments, and theoretical predictions based on the IA+MEC (Schiavilla *et al.* [10, 11]) and the dimensional-scaling quark model (DSQM, Brodsky and Chertok [25, 52]). The DSQM curve is arbitrarily normalized at $Q^2 = 50$ fm^{-2}.

Figure 14 shows the sensitivity limit for the ^{3}He $F(Q^2) \equiv \sqrt{A(Q^2)}$ form factor. The sensitivity limit is defined as the lowest form factor value that can be measured with $\sim \pm 30\%$ statistical error in four days of beam time at a given Q^2 kinematics. The experiment will be able to provide precise $F(Q^2)$ data for ^{3}He over the Q^2 range of the previous SLAC

measurements and beyond. The latter measurements [35] were performed at a single forward scattering angle ($\Theta = 8^\circ$) and were not able to separate the two form factors. Shown also in the Figure are the complete (IA+MEC) calculation of Schiavilla and collaborators [10, 11], and the prediction of the dimensional-scaling quark model (DSQM) of Brodsky and Chertok [25], arbitrarily normalized at ~ 50 fm^{-2}. The existing $F(Q^2)$ data for ^{3}He strongly suggest a change of slope at about $Q^2 = 55$ fm^{-2}, that can be attributed to a possible diffraction minimum, or to the onset of quark-dimensional scaling as argued by Chertok [52].

Figure 15 shows the quality of the projected data for the ^{4}He charge form factor, assuming (arbitrarily) a linear extrapolation of the existing data, along with theoretical predictions at large momentum transfers. The variational Monte Carlo calculations by Wiringa [12] and Schiavilla *et al.* [11] and the correlated-hyperspherical harmonics variational method calculation by Marcucci *et al.* [45], shown in the Figure, predict a second diffraction minimum that would be measurable by this experiment. Also shown in the Figure is the asymptotic prediction of the dimensional-scaling quark model by Brodsky and Chertok [25], arbitrarily normalized at ~ 40 fm^{-2}. The estimated cross sections, counting rates, running times and projected statistical uncertainties in the extraction of the ^{4}He form factor are given in appended Table 5.

It is evident, from Figures 12, 13, 14 and 15, that this experiment will significantly advance our knowledge of the form factors of the three- and four-body systems. The expected data will extend our ^{3}He and ^{4}He form factor knowledge down by one to two orders in magnitude and out in Q^2 by possibly more than a factor of two. The run plan scenarios of Tables 4 and 5 amount to a required beam time, for each form factor measurement, of 12 days (including 2 days of proton calibrations and empty target runs). The total requested amount of beam time for the experiment is 36 days. The proposed measurements will be able to uncover the predicted second diffraction minima of the ^{3}He and ^{4}He form factors or explore a possible asymptotic fall off indicative of a transition from meson-nucleon to quark-gluon degrees of freedom in the few-body form factor description.

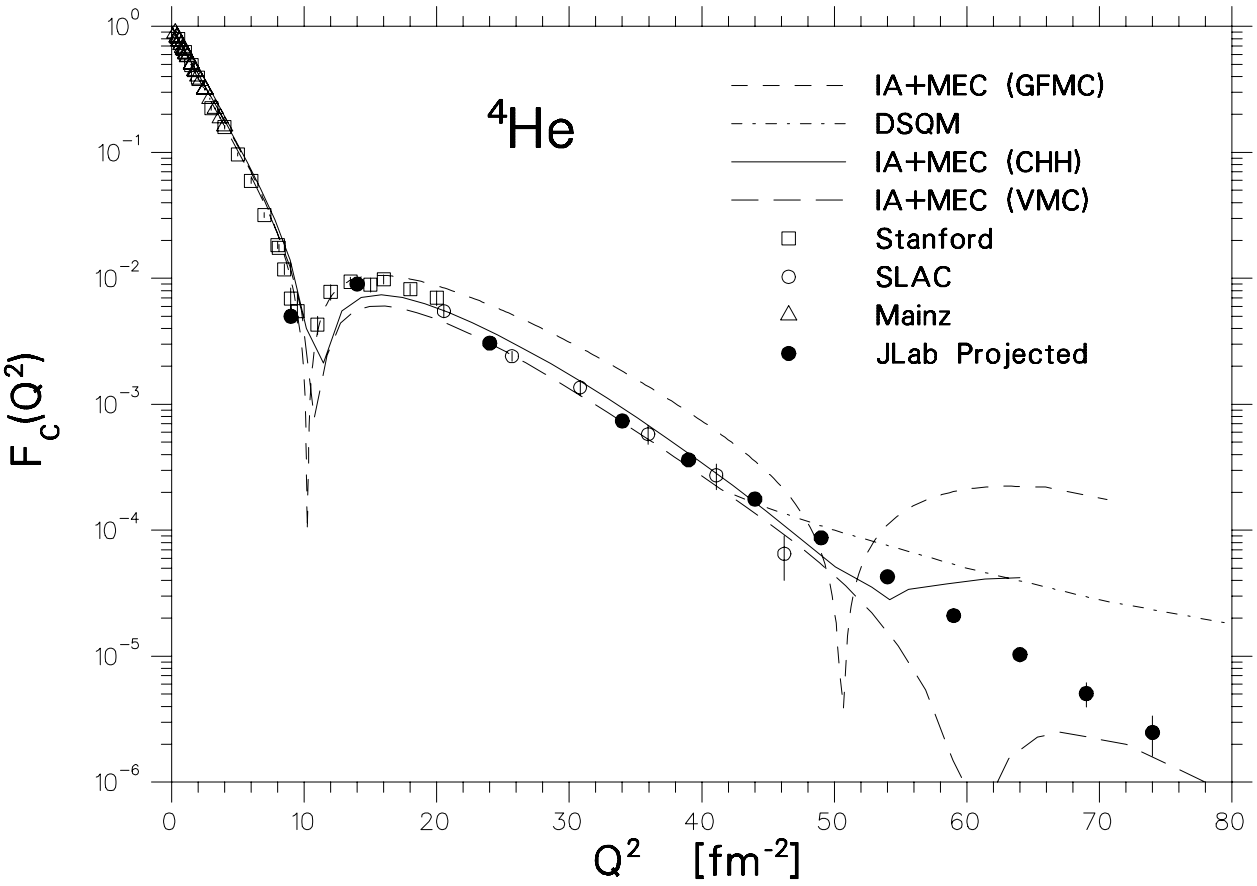

Figure 15: ^{4}He charge form factor projected data from this experiment along with the existing Stanford [27, 44], Mainz [34] and SLAC [35] data. Also shown are variational Monte Carlo (VMC), Green's Function Monte Carlo (GFMC) and correlated-hyperspherical harmonics variational method (CHH) calculations by Schiavilla *et al.* [11], Wiringa [12] and Marcucci *et al.* [45], respectively, along with the prediction of the dimensional-scaling quark model (DSQM) of Brodsky and Chertok [25, 52]. The DSQM curve is arbitrarily normalized at $Q^2 = 40$ fm^{-2}.

4 Summary

In summary, this is a proposal to measure the charge and magnetic form factors of ^{3}He and the charge form factor of ^{4}He up to the largest momentum transfers possible in the JLab Hall A Facility. We request 36 days of beam time with beam energies between 0.8 and 4.4 GeV and beam current of 100 μA for helium production data, and hydrogen calibrations and

monitoring. The expected data will extend our three- and four-body form factor knowledge down by one to two orders in magnitude and out in Q^2 by possible more than a factor of two. The experiment will produce data of fundamental importance for our understanding and advancement of modern few-body nuclear physics, provide invaluable input for the establishment of a consistent hadronic model for the description of the electromagnetic interaction with the few-body systems, and test long-standing predictions of quark-dimensional scaling for the few-body form factors.

Acknowledgement: We are grateful to Professors F. Gross, A. Stadler and M. T. Peña for the kind communication of their paper on the three-body covariant spectator theory prior to submission for publication.

^{3}He Forward Kinematics

Q^2 (fm^{-2})	E (GeV)	E' (GeV)	Θ (deg.)	P_r (GeV/c)	Θ_r (deg.)	$(\Delta\Omega)_e/(\Delta\Omega)_r$
20.0	4.0	3.861	12.9	0.893	74.7	0.20
30.0	4.0	3.792	16.0	1.101	71.2	0.26
39.5	4.0	3.726	18.5	1.270	68.5	0.32
48.0	4.4	4.067	18.6	1.407	67.2	0.31
59.0	4.4	3.991	20.8	1.570	64.7	0.36
66.0	4.4	3.942	22.2	1.667	63.3	0.40
75.5	4.4	3.877	24.0	1.793	61.4	0.45
85.0	4.4	3.811	25.7	1.912	59.7	0.50

Table 1: Incident beam, scattered electron and recoil nucleus kinematics for the forward ^{3}He measurements (the kinematical variables are defined in the text).

^{3}He Backward Kinematics

Q^2 (fm^{-2})	E (GeV)	E' (GeV)	Θ (deg.)	P_r (GeV/c)	Θ_r (deg.)	$(\Delta\Omega)_e/(\Delta\Omega)_r$
20.0	0.80	0.661	74.7	0.893	45.6	2.61
30.0	0.80	0.592	103.5	1.101	31.5	4.06
39.5	0.80	0.526	145.8	1.270	13.5	5.99
48.0	0.90	0.567	146.2	1.407	13.0	6.31
59.0	1.10	0.691	120.7	1.570	22.2	5.58
66.0	1.10	0.642	144.9	1.667	12.8	6.90
75.5	1.20	0.677	144.1	1.793	12.8	7.20
85.0	1.30	0.711	142.3	1.912	13.1	7.43

Table 2: Incident beam, scattered electron and recoil nucleus kinematics for the backward ^{3}He measurements (the kinematical variables are defined in the text).

^{4}He Kinematics

Q^2 (fm^{-2})	E (GeV)	E' (GeV)	Θ (deg.)	P_r (GeV/c)	Θ_r (deg.)	$(\Delta\Omega)_e/(\Delta\Omega)_r$
9.0	2.2	2.153	15.6	0.594	77.7	0.36
14.0	3.3	3.227	13.0	0.742	77.9	0.25
24.0	3.3	3.175	17.2	0.975	74.1	0.34
34.0	3.3	3.122	20.7	1.164	71.0	0.43
39.0	3.3	3.096	22.2	1.249	69.7	0.47
44.0	3.3	3.070	23.7	1.329	68.4	0.51
49.0	3.3	3.044	25.2	1.405	67.2	0.55
54.0	4.4	4.118	19.6	1.477	69.3	0.37
59.0	4.4	4.092	20.6	1.547	68.4	0.39
64.0	4.4	4.066	21.5	1.614	67.5	0.41
69.0	4.4	4.040	22.4	1.678	66.6	0.44
74.0	4.4	4.013	23.3	1.741	65.8	0.46

Table 3: Incident beam, scattered electron and recoil nucleus kinematics for the ^{4}He measurements (the kinematical variables are defined in the text).

^{3}He Run Plan

Q^2 (fm^{-2})	$[d\sigma/d\Omega)]_f$ (nb/sr)	N_f	T_f (h)	$[d\sigma/d\Omega)]_b$ (nb/sr)	N_b	T_b (h)	F_C	ΔF_C ($\pm$%)	F_M	ΔF_M ($\pm$%)
20.0	1.7E-1	131072	2	2.7E-3	131072	45	4.7E-3	0.2	1.6E-3	13
30.0	1.6E-2	8192	1	1.3E-4	2048	13	2.2E-3	0.7	8.9E-4	15
39.5	1.1E-3	2048	3	2.2E-6	128	18	8.0E-4	1.2	2.9E-4	12
48.0	8.4E-5	512	12	1.5E-7	32	68	2.5E-4	2.4	7.3E-5	26
59.0	2.2E-6	32	23	6.3E-8	16	130	2.7E-5	50	7.4E-5	15
66.0	4.9E-6	64	18	9.0E-8	8	28	6.2E-5	23	1.0E-4	19
75.5	4.0E-6	64	20	7.6E-8	8	34	6.8E-5	20	9.5E-5	20
85.0	2.0E-6	32	18	4.5E-8	8	58	5.4E-5	26	7.6E-5	20

Table 4: A run plan scenario for the ^{3}He forward (f) and backward (b) measurements, assuming that the charge and magnetic form factors follow a model by Schiavilla and collaborators [10, 11]. Here, N and T denote the expected number of elastic events and the required beam time, respectively. The form factor errors represent statistical uncertainties.

^{4}He Run Plan

Q^2 (fm^{-2})	$d\sigma/d\Omega$ (nb/sr)	T (h)	N	F_C	ΔF_C ($\pm$%)
9.0	3.0E-1	0.1	128000	5.0E-3	0.1
14.0	9.1E-1	0.1	390000	9.0E-3	0.1
24.0	3.4E-2	0.3	43000	3.1E-3	0.2
34.0	9.2E-4	0.5	18000	7.4E-4	0.4
39.0	1.6E-4	1	700	3.6E-4	2
44.0	3.0E-5	2	200	1.8E-4	4
49.0	5.6E-6	4	100	8.7E-5	5
54.0	2.1E-6	8	70	4.3E-5	6
59.0	4.2E-7	16	30	2.1E-5	9
64.0	8.3E-8	38	14	1.0E-5	13
69.0	1.7E-8	68	5	5.1E-6	22
74.0	3.5E-9	102	2	2.5E-6	35

Table 5: A run plan scenario for the ^{4}He measurements, assuming that the charge form factor is described by a linear extrapolation of the existing SLAC data [35]. Here, N and T denote the expected number of single-arm elastic events and the required beam time, respectively. The form factor error is statistical.

APPENDIX

A1: The Coincidence Elastic Cross Section

In a single-arm elastic electron-nucleus experiment, where only the scattered electron is detected, the number N_e of elastically scattered electrons in the interval $\Delta E' = E'_{max} - E'_{min}$ around the elastic peak is:

$$N_e = N_b N_t C \frac{d\sigma}{d\Omega}(E_\circ, \Theta_\circ) exp[\delta(\Delta E')] \chi(\Delta E') \Delta\Omega, \tag{7}$$

where $d\sigma(E_\circ, \Theta_\circ)/d\Omega$ is the elastic cross section of interest for the central values of $E_\circ$ and $\Theta_\circ$, N_b is the number of incident beam electrons, N_t is the number of target nuclei per cm^2, C contains all applicable corrections including the detector inefficiencies and dead-time effects, and $\Delta\Omega$ is the electron spectrometer solid angle. The factor $exp[\delta(\Delta E')]$ accounts for losses due to radiation effects (radiative correction factor) and it is calculable analytically when the spectrometer energy acceptance $\Delta E'$ is independent of the electron scattering angle Θ. The factor $\chi(\Delta E')$ (ionization factor) accounts for losses due to ionization effects and for high energies becomes approximately multiplicative and equal to $(1 - \xi/\Delta E')$, where the parameter ξ is characteristic of the target material (see below).

In a double-arm experiment, the number of electrons N_{er} in coincidence with recoil nuclei detected in a recoil spectrometer in the interval $\Delta P_r = (P_r)_{max} - (P_r)_{min}$ is:

$$N_{er} = N_b N_t C \frac{d\sigma}{d\Omega}(E_\circ, \Theta_\circ) exp[\delta(\Delta E', \Delta P_r)] \chi(\Delta E', \Delta P_r) \Delta\Omega_{er}, \tag{8}$$

where in this case the radiative correction factor and the ionization factor depend on both $\Delta E'$ and ΔP_r, the solid angle becomes the effective double-arm solid angle $\Delta\Omega_{er}$, and the correction factor C includes also losses due to absorption of recoil nuclei in the target and the detectors. The radiative correction factor is calculable only if one of the two spectrometers is the limiting aperture defining the double-arm solid angle, and if the recoil spectrometer momentum acceptance ΔP_r is independent of the recoil angle Θ_r. In practice, even if the latter condition is met, in a realistic experiment where counting rate limitations dictate use of the maximum solid angle available from a double-arm spectrometer system, the effective double-arm solid angle is in many kinematics defined, as it is the case for this experiment,

by both spectrometers. The resulting convolution of the solid angles of the two spectrometers, coupled by elastic kinematics and radiative and ionization effects makes impossible the calculation of the product $exp[\delta(\Delta E', \Delta P_r)]\chi(\Delta E', \Delta P_r)\Delta\Omega_{er}$ analytically. The product, in this case, has to be calculated by means of a Monte Carlo simulation.

To express the above convolution, one has to write down the coincidence counting rate as:

$$N_{er} = N_b N_t C \left\langle \int\int \frac{d\sigma_{exp}}{d\Omega dE'}(E, E', \Theta, t)\Delta\Omega\Delta E' \right\rangle_{E,L}, \tag{9}$$

where $d\sigma_{exp}(E, E', \Theta, t)/d\Omega dE'$ is the differential experimental cross section, which depends also on the position, t, of the scattering vertex of the elastic event along the target length L. The experimental cross section is integrated over the effective angular and scattered electron energy acceptances of the double-arm spectrometer system for detection of scattered electrons in coincidence with recoil nuclei. The bracket enclosure indicates that the resulting integral is averaged over the energy distribution of the incident beam and over the length of the target.

A2: Monte Carlo Simulation

The above averaged integral has to be calculated by simulating the entire elastic electron-nucleus scattering process, starting with the arrival of the beam electrons at the target, and ending with the arrival of the scattered electrons and of the recoil nuclei at the detectors of the electron and recoil spectrometer, respectively. The simulation requires complete knowledge of all physical processes happening in the target, in addition to the elastic scattering process in question, and transportation of scattered and recoil particles through reliable optical models of the spectrometers used for their detection. Among all processes present, the dominant one is radiation by the incoming and scattered electrons, which is inextricably interwind with the scattering process.

A2.1: Internal and External Bremsstrahlung

There are two kinds of radiation effects. The first one is from real and virtual photons emitted during the elastic scattering (referred to as internal bremsstrahlung and vertex corrections respectively). The second one is from real photons emitted by electrons when

passing through the target material before and after the scattering (referred to as external bremsstrahlung).

Following the seminal papers by Mo and Tsai [53, 54], and neglecting for the time being ionization energy loss effects, the cross section for electrons of incident energy E to scatter at an angle Θ to a final energy E' from a target of T radiation lengths including all radiation effects is given by:

$$\frac{d\sigma_{exp}}{d\Omega dE'} = \int_{\circ}^{T} \frac{dt}{T} \int_{\eta' E'}^{E} dE_1 \int_{E'}^{\eta_1 E_1} dE_1' \; I_e(E, E_1, t) \; \frac{d\sigma}{d\Omega dE'}(E_1, E_1', \Theta) \; I_e(E_1', E', T-t), \quad (10)$$

where $I_e(E, E_1, t)$ is the probability of finding an electron starting at initial energy E and straggling down to energy E_1 after passing through t radiation lengths in the target, $I_e(E_1', E', T-t)$ is the probability of finding an electron after the scattering at energy E_1' and straggling down to energy E' through the rest of the target, and $d\sigma(E_1, E_1', \Theta)/d\Omega dE'$ is the cross section for elastic scattering with incident energy E_1 to final energy E_1' and at an angle Θ including internal radiation and vertex corrections. The lower limit of integration for E_1 is $\eta' E'$ and the upper limit of integration for E_1' is $\eta_1 E_1$, where $\eta' = [1 - 2(E'/M)\sin^2(\theta/2)]^{-1}$ and $\eta_1 = [1 + 2(E_1/M)\sin^2(\theta/2)]^{-1}$. The difference $E - \eta' E'$ is the maximum energy of a photon which can be emitted along the direction of the incident electron. Similarly the maximum energy of a photon which can be emitted along the direction of the scattered electron is $\eta E - E'$, where $\eta = [1 + 2(E/M)\sin^2(\theta/2)]^{-1}$.

It is customary, in addition to using the angle peaking approximation, to assume that the shape of the internal bremsstrahlung is the same as that of the external bremsstrahlung, and that the internal bremsstrahlung has approximately the same effect as that given by two "external equivalent radiators" with one placed before and one after the scattering, each of thickness:[1]

$$t_{eq} = \frac{1}{b}\frac{\alpha}{\pi}\left[\ln\frac{Q^2}{m_e^2} - 1\right], \quad (11)$$

where m_e is the electron mass, and the small terms proportional to Z and Z^2 from radiation

[1]For clarity of the formulation a factor b^{-1} has been included in the definition of the equivalent radiator.

by the target nucleus with atomic number Z are neglected. The quantity b is approximately equal to 4/3 and depends only weakly on Z:

$$b = \frac{4}{3}\{1 + \frac{1}{9}[\frac{(Z+1)}{(Z+\zeta)}][\ln(183Z^{-\frac{1}{3}})]^{-1}\}, \tag{12}$$

where:

$$\zeta = \frac{\ln(1440Z^{-\frac{2}{3}})}{\ln(183Z^{-\frac{1}{3}})}. \tag{13}$$

The vertex corrections are included in the factor $F(Q^2, 0) = 1 + \delta'$, where:

$$F(Q^2, T) = 1 + 0.577bT + \frac{2\alpha}{\pi}\left[-\frac{14}{9} + \frac{13}{12}\ln\frac{Q^2}{m_e^2}\right] - \frac{\alpha}{2\pi}\ln^2(\frac{E}{E'}) - \frac{\alpha}{\pi}\left[\frac{\pi^2}{6} - \Phi(\cos^2\frac{\theta}{2})\right], \tag{14}$$

with $\Phi\left[\cos^2(\frac{\theta}{2})\right]$ being the Spence function. The first two terms of the right-hand side come from a Gamma function normalization factor $1/\Gamma(1+bT) \simeq 1 + 0.5772bT$. The third term is the sum of the vacuum polarization and the non-infrared part of the vertex correction. The fourth term can be regarded as a correction to the peaking approximation in the internal bremsstrahlung. The fifth term comes from the non-infrared divergent part of the soft photon emission cross section.

The probability of a small energy loss $E_i - E_f$ due to bremsstrahlung by an electron with incident energy $E_i > 100$ MeV in a target of t radiation lengths is given by:

$$I_e(E_i, E_f, t) = \frac{bt}{\Gamma(1+bt)}\left(\frac{E_i - E_f}{E_i}\right)^{bt}\frac{1}{E_i - E_f}. \tag{15}$$

Application of Equation 10 for an effective radiator of length $T_b = t_b + t_{eq}$, before the scattering, and an effective radiator of length $T_a = t_a + t_{eq}$, after the scattering, where t_b and t_a are the real radiator lengths before and after the scattering, and insertion of the vertex correction factor $(1 + \delta')$ results to:

$$\frac{d\sigma_{exp}}{d\Omega dE'} = \int_{\eta' E'}^{E} dE_1 I'_e(E, E_1, T_b)\frac{d\sigma}{d\Omega}(E_1, \Theta)(1+\delta')I'_e(\eta_1 E_1, E', T_a), \tag{16}$$

where the function $I'_e(E_i, E_f, T_j)$ is given (for $j = a, b$) by:

$$I'_e(E_i, E_f, T_j) = \frac{bT_j}{\Gamma(1+bt_j)}\left(\frac{E_i - E_f}{E_i}\right)^{bT_j}\frac{1}{E_i - E_f}. \tag{17}$$

The calculation is straightforward but messy and uses the presence of a delta function for elastic scattering:

$$\frac{d\sigma}{d\Omega dE'}(E_1, E_1', \Theta) = \frac{d\sigma}{d\Omega}(E_1, \Theta)\frac{E_1}{E_1'}\ \delta\left[E_1 - E_1' - \frac{2E_1E_1'}{M}\sin^2(\frac{\Theta}{2})\right] \tag{18}$$

Setting $d\sigma(E_1, \Theta)/d\Omega = w(E_1, \Theta)d\sigma(E_\circ, \Theta_\circ)/d\Omega$, and using basic properties of the Gamma function, the experimental cross section becomes:

$$\frac{d\sigma_{exp}}{d\Omega dE'} = \frac{d\sigma}{d\Omega}(E_\circ, \Theta_\circ)F(Q^2, T)G(E, E', \Theta, t) \tag{19}$$

where $T = t_a + t_b$ and:

$$G(E, E', \Theta, t) = \int_{\eta' E'}^{E} dE_1 g(E, E', E_1, \Theta, t) \tag{20}$$

with:

$$g(E, E', E_1, \Theta, t) = \frac{bT_b}{E - E_1}\left(\frac{E - E_1}{E}\right)^{bT_b} w(E_1, \Theta)\frac{bT_a}{E_1 - E'}\left(\frac{\eta_1 E_1 - E'}{E'}\right)^{bT_a}, \tag{21}$$

where the factor $F(Q^2, T)$ is a very slow varying function of Q^2 and has been pulled out of the integral.

Direct substitution of Equation 19 into Equation 9 results in Equation 5 of the main text:

$$\frac{d\sigma}{d\Omega}(E_\circ, \Theta_\circ) = \frac{N_{er}}{N_b N_t C F(Q^2, T) P_{MC}}, \tag{22}$$

where:

$$P_{MC} = \left\langle \int\int G(E, E', \Theta, t) d\Omega dE' \right\rangle_{E,L}. \tag{23}$$

The above analysis indicates that the determination of the product of the double-arm solid angle and the radiative corrections is reduced to a simulation of the complex integral of Equation 20. Equation 21 suggests that the internal and external bremsstrahlung of an incident or scattered electron, with initial energy E_i, in a total (real and equivalent) radiator thickness T', follows a probability distribution of the functional form:

$$\frac{bT'}{\Delta E_{if}}\left(\frac{\Delta E_{if}}{E_i}\right)^{bT'}, \tag{24}$$

where ΔE_{if} is the energy loss by the electron. The term $w(E_1, \Theta)$ dictates that a simulation of an electron-nucleus scattering event must be weighted by a probability distribution defined

by the elastic cross section. Since the elastic cross section is to be measured, one has to use a model for it, then determine P_{MC} and subsequently the elastic cross section, and after that iterate. The procedure converges very quickly.

The factor P_{MC} is essentially a number that can be determined from a Monte Carlo model that can simulate in the nuclear target material not only energy losses due to internal and external bremsstrahlung of the incident and scattered electrons, but also ionization energy losses and multiple scattering effects for the incident and scattered electrons and for the recoil nuclei.

A2.2: Ionization Energy Losses

The energy loss of charged particles due to ionization or excitation of the atoms of the material they traverse is subject to appreciable fluctuations about the most probable energy loss ΔE_{prob}. Ionization energy losses by the incident and scattered electrons, and by the recoil nuclei cannot be neglected in this experiment. The most probable energy loss is given by [55]:

$$\Delta E_{prob} = \frac{2\pi n e^4 z^2 t}{m_e c^2 \beta^2 \rho}\left[\ln \frac{4\pi n e^4 z^2 t}{I^2(1-\beta^2)\rho} - \beta^2 + 0.198 - \delta - U\right] \tag{25}$$

where n is the volume density of electrons in the material, ρ is the density of the material, I is the mean excitation potential of the material, z is the charge of the incident particle in unis of the electron charge e, t is the path length of the particle in the material, and $\beta = v/c$, where v is the velocity of the particle. The term δ is the correction for the density effect, which is due to the polarization of the medium. The term U is due to the nonparticipation of the inner shels (K, L,...) for very low velocities of the incident particle.

The shape of the ionization energy loss distribution depends on the value of the parameter $K = \xi/q_{max}$ [56, 57], where:

$$\xi = \frac{2\pi z^2 e^4 n t}{m_e v^2} \tag{26}$$

and q_{max} is the maximum energy transfer in the collision from the incident particle to the atomic electrons, approximately given by $2m_e v^2/(1-\beta^2)$ for incident heavy particles and by $T_e/2$ for incident electrons, where T_e is the kinetic energy of the electron.

There is no absolute K demarcation defining the shape of the energy loss distribution. For the needs of this experiment it is sufficient to consider that for $K > 0.2$ the energy

loss follows a Gaussian distribution and for $K < 0.2$ it follows the Landau distribution [58] (in reality, for $0.01 < K < 1.0$ the energy loss follows the Symon distribution [59, 60], but application of his theory to a specific case is difficult without considerable manipulation and extrapolation of his unpublished results).

The variance, σ_i^2, of the Gaussian distribution is given in terms of the path length t of the particle in the material as [56]:

$$\sigma_i{}^2 = 4\pi e^4 n z^2 t. \tag{27}$$

The Landau distribution is asymmetric with a long high-energy loss tail and a broad peak. If ΔE is the observed energy loss, Landau has described the distribution as:

$$\Phi(\lambda) = \int_{-i\infty}^{+i\infty} exp[\lambda u + u \ln u] du \tag{28}$$

where the parameter λ is given in terms of the parameter ξ and the most probable energy loss as $\lambda = (\Delta E - \Delta E_{prob})/\xi$.

A2.3: Multiple Scattering Effects

Another effect that has to be taken into account in a simulation of electron-nucleus scattering is the multiple scattering of the incident and scattered electrons and of the recoil nuclei in the Coulomb field of the nuclei of the target materials. It contributes to the value of the integral P_{MC} and to a larger extend to the shape of the observed distributions of the scattered electrons and of the recoil nuclei at the detectors. A reliable comparison between observed and simulated detector distributions would not be possible without incorporation of multiple scattering in the Monte Carlo model.

The resultant distribution of the net space angle θ between the incoming and outgoing directions of the particle, after passing a material of thickness t, is a Gaussian-type distribution with a long non-Gaussian tail below the 5% level. The mean square value of θ is given by [61]:

$$\langle \theta^2 \rangle^{\frac{1}{2}} = \left[\frac{0.157 Z(Z+1) z^2 t}{A(pv)^2} \ln \left[1.13 \times 10^4 Z^{\frac{4}{3}} z^2 t A^{-1} \beta^{-2} \right] \right]^{\frac{1}{2}} \tag{29}$$

where p is the momentum of the incident particle and A is the mass number of the material. The multiple scattering angular distribution is in practice approximated by a Gaussian function. There is no unique parametrization for the standard deviation, σ_{ms}, of such a

Gaussian distribution. The best approximate formula, working very well, especially for small-Z materials, is given by Lynch and Dahl as [62]:

$$\sigma_{ms} = \frac{19.2z}{p\beta}\sqrt{\frac{X}{X_\circ}}\left[1 + 0.088\log_{10}(\frac{z^2X}{\beta X_\circ})\right], \tag{30}$$

where X and $X_\circ$ are the thickness and radiation length of the material, respectively.

A2.4: Transportation of Particles through the Spectrometers

The Monte Carlo model, after simulating the production of elastic events in the target, raytraces the scattered electrons and the recoil nuclei all the way to the detectors, through the electron and recoil spectrometers, respectively. This requires knowledge of the optical properties of the two magnetic spectrometers as determined from detailed magnetic measurements of their elements, and of the apertures of the elements as determined from surveys. The scattered electrons and the recoil nuclei are transported through the spectrometers in our model by means of exact raytrace or forward TRANSPORT matrix elements [63]. Exact raytrace (good to all orders in the TRANSPORT coordinates) is applied for the motion of the particles in the quadrupoles of the High Resolution Spectrometers. The raytrace uses the Lorentz force equation:

$$\frac{d\vec{p}}{dt} = q(\vec{v} \times \vec{B}), \tag{31}$$

where q is the charge of the particle and $\vec{B}$ is the magnetic field. The 3-dimensional magnetic field $\vec{B}$ is provided by the measured field maps $B_x(x,y,z), B_y(x,y,z), B_z(x,y,z)$ of the HRS quadrupoles. The propagation of the particles through the quadrupoles is done in small steps. At the end of each step a check is made to see whether the particles are lost on the physical apertures of the quadrupoles. For the transportation of the particles through the HRS dipoles this exact method cannot be applied due to the lack of a complete field map of the dipoles. Instead a TRANSPORT model for each dipole was created based on a combination of limited magnetic measurements and TOSCA simulations. The HRS dipole has been divided in 10 pieces, and 10 sets of 3rd-order forward matrix elements have been provided by the TRANSPORT code [64].

The forward matrix elements of a magnetic element are the coefficients of a Taylor expansion about the central trajectory of the coordinates x, θ, y, ϕ of the particle at the exit of the element in terms of its coordinates $x_\circ, \theta_\circ, y_\circ, \phi_\circ$ at the entrance of the element:

$$x = \sum_{\kappa,\lambda,\mu,\nu,\xi} (x \mid x_\circ^\kappa y_\circ^\lambda \theta_\circ^\mu \phi_\circ^\nu \delta_\circ^\xi) x_\circ^\kappa y_\circ^\lambda \theta_\circ^\mu \phi_\circ^\nu \delta_\circ^\xi \tag{32}$$

$$\theta = \sum_{\kappa,\lambda,\mu,\nu,\xi} (\theta \mid x_\circ^\kappa y_\circ^\lambda \theta_\circ^\mu \phi_\circ^\nu \delta_\circ^\xi) x_\circ^\kappa y_\circ^\lambda \theta_\circ^\mu \phi_\circ^\nu \delta_\circ^\xi \tag{33}$$

$$y = \sum_{\kappa,\lambda,\mu,\nu,\xi} (y \mid x_\circ^\kappa y_\circ^\lambda \theta_\circ^\mu \phi_\circ^\nu \delta_\circ^\xi) x_\circ^\kappa y_\circ^\lambda \theta_\circ^\mu \phi_\circ^\nu \delta_\circ^\xi \tag{34}$$

$$\phi = \sum_{\kappa,\lambda,\mu,\nu,\xi} (\phi \mid x_\circ^\kappa y_\circ^\lambda \theta_\circ^\mu \phi_\circ^\nu \delta_\circ^\xi) x_\circ^\kappa y_\circ^\lambda \theta_\circ^\mu \phi_\circ^\nu \delta_\circ^\xi \tag{35}$$

where the order n of the expansion is : $n = \kappa + \lambda + \mu + \nu + \xi$ (=3 in this case). The coordinates x and y represent, respectively, the horizontal and vertical positions of the particle, and $\theta = dx/dz$ and $\phi = dy/dz$ are the associated angles. The quantity $\delta_\circ = (p - p_\circ)/p_\circ$ is the fractional deviation of the momentum of the particle from the central design momentum, $p_\circ$, of the system.

Each one of the 10 sets corresponds to a magnetic element starting at the entrance of the dipole and ending at a location $mL/10$ inside the dipole, where $m = 1, 2, ..., 10$, and L is the effective length of the dipole. Each set is used to transport the particle from the beginning of the dipole to the $mL/10$ longitudinal position inside the dipole, where an aperture check is made to see whether the particle is lost on the trapezoidal aperture of the dipole. When the particle makes it through the aperture for the 10th step, it is traced through the third HRS quadrupole. All losses of particles on the apertures are recorded and a complete picture is obtained for the solid angle defining apertures of both spectrometers.

A2.5: The Effective Double-Arm Solid Angle

The Monte Carlo simulation creates pairs of scattered electrons and recoil nuclei along the beam direction in the target. The incident beam distribution is assumed to be of a Gaussian form with given standard deviation. Each scattering event originates from a beam electron that has undergone energy straggling through the target and has been multiple-scattered before it interacts elastically with a nucleus. The location of the scattering vertex in the target is uniformly distributed over the target length. Elastic electron events are created with polar and azimuthal angles θ and ϕ in the intervals (θ_1, θ_2) and (ϕ_1, ϕ_2) around the

electron spectrometer axis (with $\Delta\theta = \theta_1 - \theta_2$ and $\Delta\phi = \phi_1 - \phi_2$ larger than the angular acceptances of the electron spectrometer). The recoil nucleus momentum and polar and azimuthal angles are determined by the elastic scattering condition. All the kinematical coordinates of both particles are corrected, before they enter the respective spectrometer models, for energy straggling and multiple scattering on the way out through the target.

All probability distributions involved in the simulation like the ones for internal and external bremsstrahlung, ionization energy loss, multiple scattering and for elastic scattering at the scattering vertex, are produced by standard Monte Carlo techniques. Random deviates from a particular distribution are generated either using the direct transformation method, where possible, or the acceptance-rejection method by von Neumann. Both methods use real numbers uniformly distributed in the interval [0,1] as provided by a (pseudo)random number generator.

In the Monte Carlo language, the above procedure makes the integral P_{MC} equivalent to an integral of the form

$$P_{MC} = \int\int \; w(E_1, \Theta) r(\Delta E', \Delta P_r) \; d\theta d\phi, \tag{36}$$

where the function $r(\Delta E', \Delta P_r)$ includes the portion of the electron radiative corrections that depend on the momentum acceptances of the two spectrometers, and effects from ionization energy losses and multiple scattering for both scattering partners. For N trial events randomly and uniformly distributed over the target length L and over the angular ranges $\Delta\theta$ and $\Delta\phi$, the integral P_{MC} is given, in the limit $N \to \infty$, by:

$$\int_{\theta_1}^{\theta_2} \int_{\phi_1}^{\phi_2} f(\theta, \phi) d\theta d\phi = \Delta\theta \Delta\phi \frac{1}{N} \sum_{i=1}^{N} f(\theta_i, \phi_i), \tag{37}$$

where:

$$f(\theta, \phi) = w(E_1, \Theta) r(\Delta E', \Delta P_r). \tag{38}$$

Since the energy losses due to radiation and ionization and the multiple scattering effects are applied for every event, the function $f(\theta, \phi)$ takes the value:

$$f(\theta, \phi) = \begin{cases} w(E_1, \Theta) & \text{for a ``good event''} \\ 0 & \text{otherwise} \end{cases} \tag{39}$$

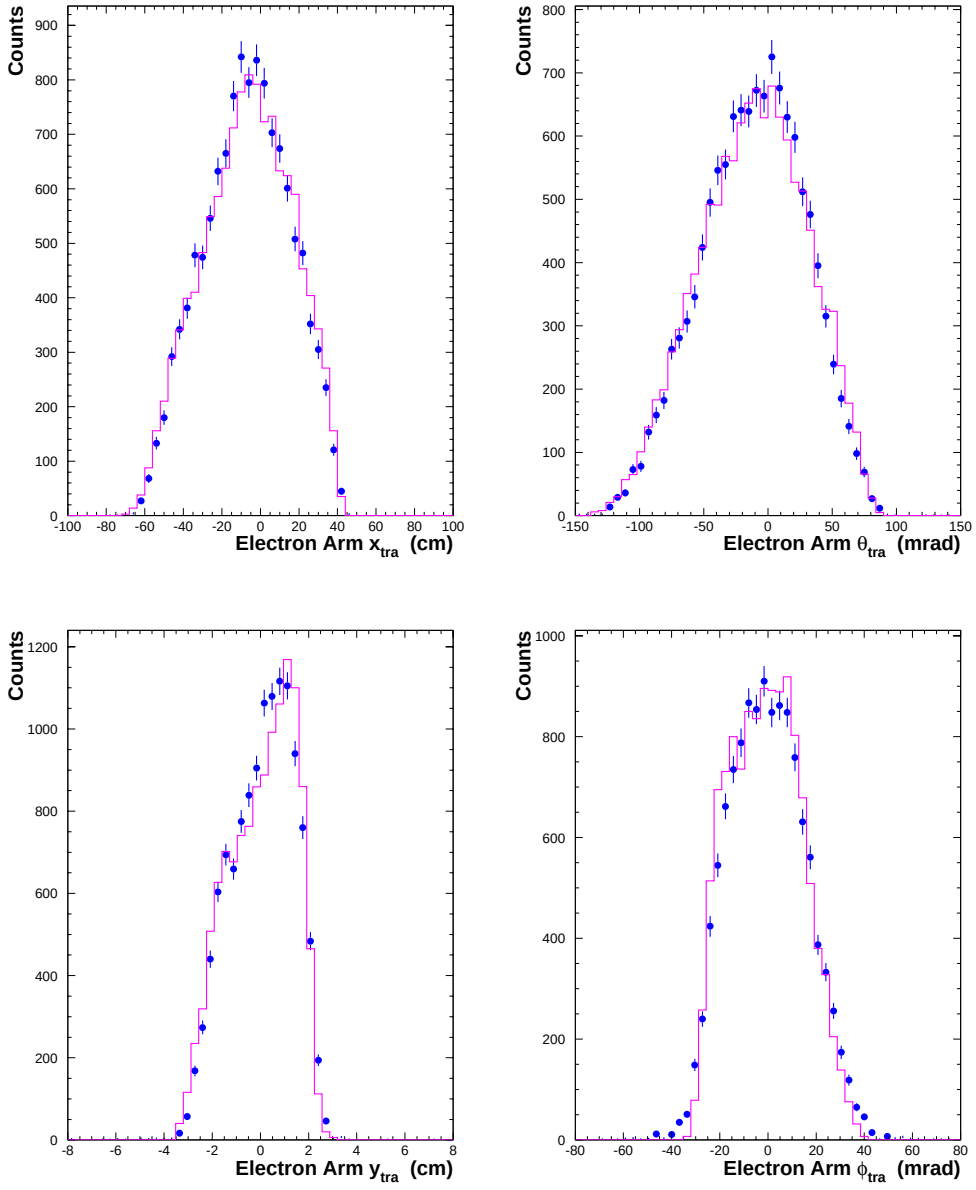

Figure 16: The JLab HRS drift chamber position and angular distributions of electrons elastically scattered off protons for one of the kinematics of experiment E91-26 (solid circles) [50]. The distributions are for coincidence events and are plotted versus the vertical (top) and horizontal (bottom) TRANSPORT position and angle coordinates. The curves represent the predictions of a Monte Carlo simulation (see text).

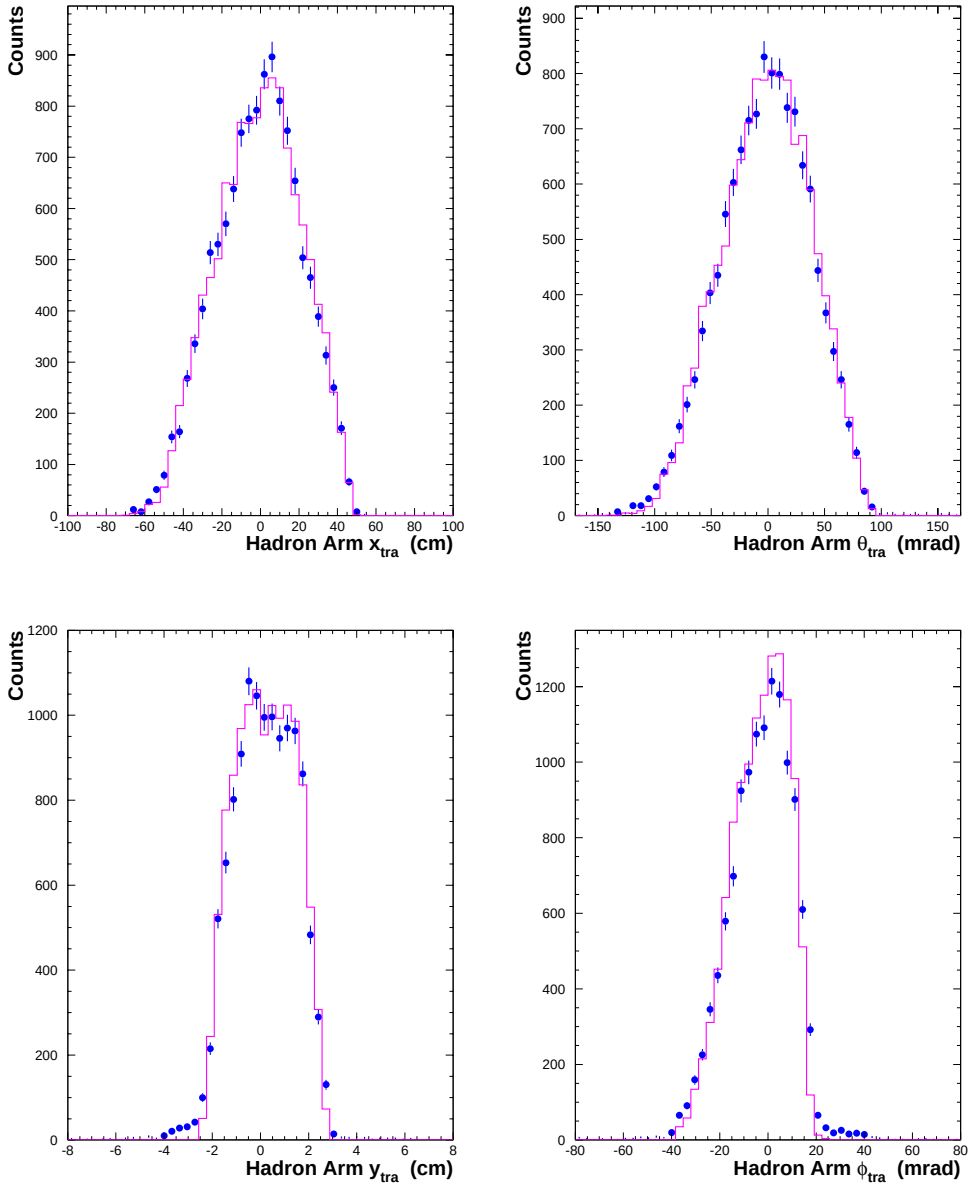

Figure 17: The JLab HRS drift chamber position and angular distributions of recoil protons for one of the elastic electron-proton kinematics of experiment E91-26 (solid circles) [50]. The distributions are for coincidence events and are plotted versus the vertical (top) and horizontal (bottom) TRANSPORT position and angle coordinates. The curves represent the predictions of a Monte Carlo simulation (see text).

where "good event" (or double-arm event) is considered the case when both the scattered electron and the recoil nucleus pass through the modeled spectrometers into the detectors without being lost on any limiting aperture. Small corrections for effects not accounted for by the above procedure, like radiation by the target nucleus, can be calculated in an approximative way by using analytic formulae. It is obvious that the same procedure can be used to calculate a corresponding integral:

$$P'_{MC} = \int\int w(E_1, \Theta) r'(\Delta E')\, d\theta d\phi \tag{40}$$

for single-arm elastic scattering with detection of only scattered electrons, which is the case for part of the ^{4}He component of the experiment.

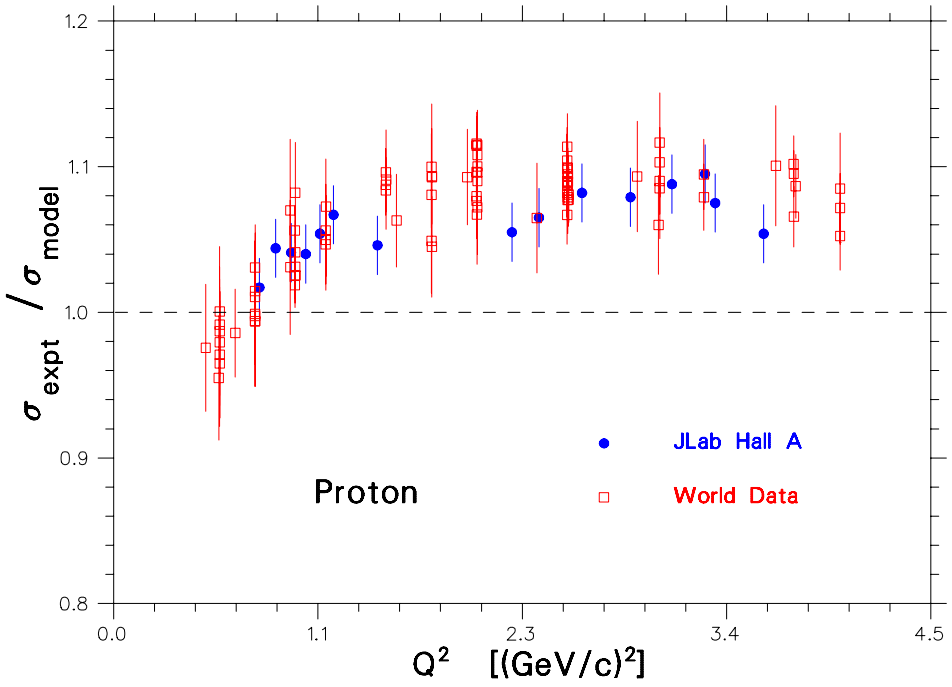

Figure 18: The elastic electron-proton cross section from JLab experiment E91-26 (measurement of the deuteron elastic structure functions) as extracted from coincidence measurements and simulation of the effective double-arm solid angle [50] compared to all previous world data for similar kinematics [65]. The experimental cross section has been divided by a model cross section assuming proton form factor scaling and using the dipole formula (see text). The JLab data include only point-to-point random errors.

This method of evaluation of the integral P_{MC} was employed in the data analysis of the measurement of the electric form factor $A(Q^2)$ of the deuteron in JLab Hall A experiment E91-26. Figures 16 and 17 show a comparison [50] of the measured distributions of the coordinates of the scattered electrons and recoil deuterons at the drift chamber locations of the two HRS detectors, for one of the E91-26 kinematics, with the distributions simulated with our Monte Carlo code. It is evident that the simulated distributions are in very good agreement with the experimental distributions giving us confidence that our Monte Carlo model describes accurately all physical processes involved in the experiment and that the product P_{MC} takes into account correctly the convolution of radiative and ionization energy loss effects with the acceptances of the two spectrometers. The integral P_{MC} was used for the determination of the coincidence elastic electron-proton and electron-deuteron cross sections. Figure 18 shows the elastic electron-proton cross section from double-arm coincidence measurements at different values of Q^2 from E91-26 [50] compared to the world data at similar kinematics [65]. To obtain a linearized scale, the experimental cross section has been divided by a cross section model assuming i) that the proton magnetic form factor follows the dipole formula $G_M^p(Q^2) = (1 + Q^2/0.71)^{-2}$ and ii) that the electric form factor is $G_E^p = G_M^p/\mu_p$ (form factor scaling), where μ_p is the proton magnetic moment. The excellent agreement of the E91-26 cross section data with the world cross section data is another indication that our Monte Carlo model calculates reliably the integral P_{MC}.

References

[1] E. Hadjimichael, in *International Review of Nuclear Physics*, Vol. 3, World Scientific, Singapore (1985).

[2] L. E. Marcucci, D. O. Riska and R. Schiavilla, Phys. Rev. **C58**, 3069 (1998).

[3] For a review see: J. Carlson and R. Schiavilla, Rev. Mod. Phys. **70**, 743 (1998).

[4] For a review see: C. E. Carlson, J. R. Hiller, R. J. Holt, Annu. Rev. Nucl. Part. Sci. **47**, 395 (1997).

[5] For a review see: I. Sick, Prog. Part. Nucl. Phys. **47**, 245 (2001).

[6] R. A. Brandenburg, Y. E. Kim and A. Tubis, Phys. Rec. **C12**, 1368 (1975).

[7] W. Strueve, Ch. Hajduk, P. U. Sauer and W. Theis, Nucl. Phys. **A465**, 651 (1987).

[8] A. Laverne and C. Gignoux, Nucl. Phys. **A203**, 597 (1973).

[9] E. Hadjimichael, B. Goulard and R. Bornais, Phys. Rev. **C27**, 831 (1983); E. Hadjimichael, Phys. Lett. **B172**, 156 (1986).

[10] R. Schiavilla, V. R. Pandharipande and D. O. Riska, Phys. Rev. **C40**, 2294 (1989); R. Schiavilla and D. O. Riska, Phys. Lett. **B244**, 373 (1990).

[11] R. Schiavilla, V. R. Pandharipande and D. O. Riska, Phys. Rev. **C41**, 309 (1990).

[12] R. B. Wiringa, Phys. Rev. **C43**, 1585 (1991).

[13] M. J. Musolf, R. Schiavilla and T. W. Donnely, Phys. Rev. **C50**, 2173 (1994).

[14] J. Carlson, Phys. Rev. **C38**, 1879 (1988).

[15] D. O. Riska, Phys. Rep. **181**, 207 (1989).

[16] A. Picklesimer, R. A. Rice and R. Brandenburg, Phys. Rev. Lett. **68**, 1484 (1992).

[17] J. Lomnitz-Adler, V. R. Pandharipande and R. A. Smith, Nucl. Phys. **A361**, 399 (1981).

[18] J. L. Friar *et al.*, Ann. Rev. Nucl. Part. Sci. **34**, 403 (1984); J. L. Friar, Nucl. Phys. **A684**, 200 (2001).

[19] T. Katayama, Y. Akaishi and H. Tanaka, Prog. Theor. Phys. **67**, 236 (1982).

[20] M. Namiki, K. Okano and N. Oshimo, Phys. Rev. **C25**, 2157 (1982).

[21] V. V. Burov and V. K. Lukyanov and A. I. Titov, Z. Phys. **A318**, 67 (1984); V. V. Burov and V. K. Lukyanov, Nucl. Phys. **A463**, 263c (1987).

[22] M. A. Maize and Y. E. Kim, Phys. Rev. **C31**, 1923 (1985).

[23] L. S. Kisslinger, W.-H. Ma and P. Hoodbhoy, Nucl. Phys. **A459**, 645 (1986); W.-H. Ma and L. S. Kisslinger, Nucl. Phys. **A531**, 493 (1991).

[24] H. Dijk and M. Beyer, Phys. Lett. **B237**, 323 (1990).

[25] S. J. Brodsky and B. T. Chertok, Phys. Rev. Lett. **37**, 269 (1976); Phys. Rev. **D14**, 3003 (1976).

[26] H. Collard *et al.*, Phys. Rev. **138**, B57 (1965).

[27] J. S. McCarthy, I. Sick and R. R. Whitney, Phys. Rev. **C15**, 1396 (1977).

[28] M. Bernheim *et al.*, Lett. Nuovo Cimento **5**, 431 (1972).

[29] J. M. Cavedon *et al.*, Phys. Rev. Lett. **49**, 987 (1982).

[30] A. Amroun *et al.*, Phys. Rev. Lett. **69**, 253 (1992); Nucl. Phys. **A579**, 596 (1994).

[31] P. C. Dunn *et al.*, Phys. Rev. **C27**, 71 (1983).

[32] D. H. Beck *et al.*, Phys. Rev. **C30**, 1403 (1984).

[33] I. Nakagawa *et al.*, Phys. Rev. Lett. **86**, 5446 (2001).

[34] C. R. Ottermann *et al.*, Nucl. Phys. **A436**, 688 (1985).

[35] R. G. Arnold *et al.*, Phys. Rev. Lett. **40**, 1429 (1978).

[36] H. Henning, P. U. Sauer and W. Theis, Nucl. Phys. **A537**, 367 (1992).

[37] G. Rupp and J. A. Tjon, Phys. Rev. **C45**, 2133 (1992).

[38] A. Stadler, F. Gross and M. Frank, Phys. Rev. **C56**, 2396 (1997).

[39] F. Gross, A. Stadler and M. T. Peña, to be submitted to Phys. Rev. **C**.

[40] F. Gross, in *Modern Topics in Electron Scattering*, ed. B. Frois and I. Sick, World Scientific, Singapore (1991); and references therein.

[41] F. Gross and D. O. Riska, Phys. Rev. **C36**, 1928 (1987).

[42] M. Garçon and J.W. Van Orden, Advances in Nucl. Phys. **26**, 293 (2001).

[43] R. Gilman and F. Gross, J. Phys. **G28**, R37 (2002).

[44] R. F. Frosch *et al.*, Phys. Rev. **160**, 874 (1967).

[45] L. E. Marcucci *et al.*, private communication.

[46] R. B. Wiringa, V. G. J. Stoks and R. Schiavilla, Phys. Rev. **C51**, 38 (1995).

[47] B. S. Pudliner, V. R. Pandharipande, J. Carlson and R. B. Wiringa, Phys. Rev. Lett. **74**, 4396 (1995).

[48] *Opportunities for Nuclear Science – A Long Range Plan for the Next Decade*, by the DOE/NSF Nuclear Science Advisory Committee, April 2002.

[49] L. C. Alexa *et al.*, Phys. Rev. Lett. **82**, 1374 (1999).

[50] K. McCormick *et al.*, The Jefferson Lab Hall A Collaboration, in preparation for submission to Phys. Rev. **C**.

[51] A. T. Katramatou *et al.*, Nucl. Instr. and Meth. **A267**, 448 (1988); and references therein.

[52] B. T. Chertok, Phys. Rev. Lett. **41**, 1155 (1978).

[53] L. W. Mo and Y. S. Tsai, Rev. Mod. Phys. **41**, 205 (1969).

[54] Y. S. Tsai, SLAC-PUB-848 (1971).

[55] R. M. Sternheimer and R. F. Peirls, Phys. Rev. **B3**, 3681 (1971).

[56] A. Crispin and G. N. Fowler, Rev. Mod. Phys. **42**, 290 (1970).

[57] U. Fano, Ann. Rev. Nucl. Sci. **13**, 1 (1960).

[58] L. D. Landau, J. Phys. U.S.S.R. **8**, 201 (1944).

[59] K. R. Symon, Ph.D. Thesis, Harvard University (1948).

[60] B. Rossi, *High Energy Particles*, Prentice-Hall, Inc., New Jersey (1961).

[61] R. M. Sternheimer, in *Methods of Experimental Physics*, Vol. 5, edited by L. C. Yuan and C. S. Wu, Academic Press, New York (1961).

[62] G. R. Lynch and O. I. Dahl, LBL Report 28165 (1990).

[63] K. L. Brown, SLAC Report 75 (1982).

[64] D. C. Carey, K. L. Brown and F. Rothacker, SLAC Report 462 (1995).

[65] L. Andivahis *et al.*, Phys. Rev. **D50**, 5491 (1994); and references therein.